Characterization of Stress Corrosion Cracking Using Laser Ultrasonics

DOT Contract No. DTPH56-06-T-000003

Final Report

August 31, 2008

Period of Performance: 04/01/06 to 08/31/08

Sponsor:
DOT/PHMSA
Washington, DC

Technical Monitor:
James Merritt
303-683-3117

Presented by:
Intelligent Optical Systems, Inc.
2520 West 237th Street
Torrance, California 90505

Principal Investigator
Marvin Klein, Ph.D.
424-263-6361

ATTACHMENT 1

Technical Status, Results, and Conclusions

1.0 INTRODUCTION

In-service inspection of gas and oil pipelines is a subject of great current interest. Issues of safety and fitness for service have driven extensive efforts to develop effective monitoring and inspection techniques. A number of effective NDT techniques have been developed for screening to identify regions of interest for more detailed evaluation. The three anomalies of greatest interest are (1) corrosion, (2) mechanical damage and (3) stress corrosion cracking (SCC). In this paper we will focus on the application of laser ultrasonics to the characterization of SCC.

Stress corrosion cracking is the phenomenon in metals wherein the simultaneous presence of tensile stress, a corrosive environment and a susceptible metallurgy leads to the nucleation and propagation of highly irregular and complex cracks, usually found in closely spaced clusters or colonies. In pipelines, SCC has been a particularly elusive and challenging problem.

Several pipeline failures around the world have been attributed to SCC since its discovery in pipelines in the 1960s. While the number of incidents attributed to SCC is less than those attributed to other threats to pipelines such as corrosion or mechanical damage, it constitutes a formidable challenge due to the following key reasons:

- No reliable and accurate inspection tools or predictive modeling based tools exist that are capable of determining what locations along the pipeline are affected by SCC.
- No reliable and widely accepted assessment tools exist for evaluation of SCC, once found.
- No reliable and widely accepted tools exist that are capable of measuring the depth of these cracks accurately.
- No generally accepted method for fitness for service evaluation of SCC exists.

2.0 STRESS CORROSION CRACKING

Stress corrosion cracking, as found in pipelines is classified into two major types based on the environments in which they are found to originate. They are: (1) high pH SCC and (2) near neutral SCC.

2.1 High pH SCC

Also known as 'classical' SCC, high pH SCC (Figure 1, left) tends to occur at locations where the immediate environment of the pipe and resulting electrolyte has a pH of between 8 and 9. This form of SCC is known to have relatively jagged crack shapes with extensive branching. Also, it is known to be more prevalent at locations along the pipeline that are subjected to higher temperatures and cyclic pressures such as downstream of a compressor station.

This form of SCC usually comprises of cracks that aligned in a direction parallel to the axis of the pipe and the colonies tend to conform to shape of the disbanded area where-in the electrolyte was trapped.

2.2 Near-Neutral SCC

This type of SCC (Figure 1, right) is also knows as low pH SCC because it is usually found to be associated with locations wherein the electrolyte found has a pH of between 5.5 and 7.5. The cracks formed by this mechanism are usually relatively straight and have been found to be associated with areas of relatively minor corrosion and at weld locations where disbonding of the coating leads to the entrapment of conducive electrolytes.

Near neutral SCC cracks are also primarily found to be oriented in a direction parallel to the axis of the pipe. However, several locations have been discovered where such cracking was found to occur in the circumferential direction. This is believed to be caused by stresses other than the hoop stress such as bending loads at bend locations.

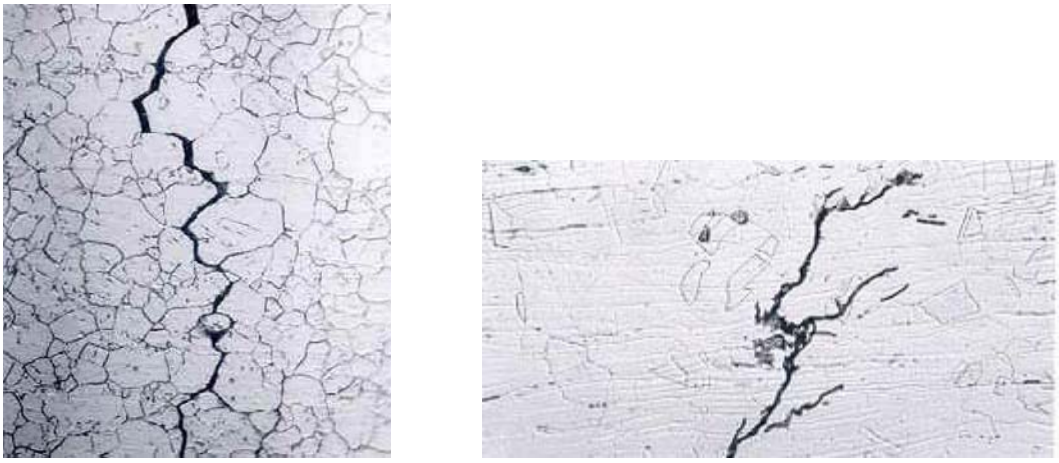

Figure 1 High pH SCC (left) and near neutral SCC (right).

2.3 Crack Characteristics

Both types of SCC share a lot of common crack characteristics. Cracks grow in both length and depth. An isolated crack would lead to a rupture if the length and depth reaches a critical length. Conversely, if a crack grows in depth at a faster pace than the length, and penetrates fully through the cross-section of the pipe before reaching a critical length, it will lead to a leak.

At times, adjacent cracks, if aligned, coalesce to form a combined or 'interlinking' crack. These interlinking cracks have a much higher length to depth ratio than the isolated cracks and therefore have a high probability of leading to a rupture.

3.0 DETECTION AND IMAGING OF SCC

Anomalies associated with colonies of SCC can sometimes be detected by in-line inspection. More commonly, Magnetic Particle Inspection (MPI) is the most widely used non-destructive method used for detection of SCC (Figure 2). A magnetic field is applied onto the surface of the pipe by means of a yoke and powdered or liquid-suspended ferromagnetic particles are introduced to the pipe surface. If there are any cracks present on the pipe surface, the ferromagnetic particles tend to accumulate at the cracks and are visible to the eye. In this way, the field-operatives can detect the presence of SCC. Furthermore, as the cracks are visible now, manual measurements of colony and crack dimensions (excluding depth) can be performed.

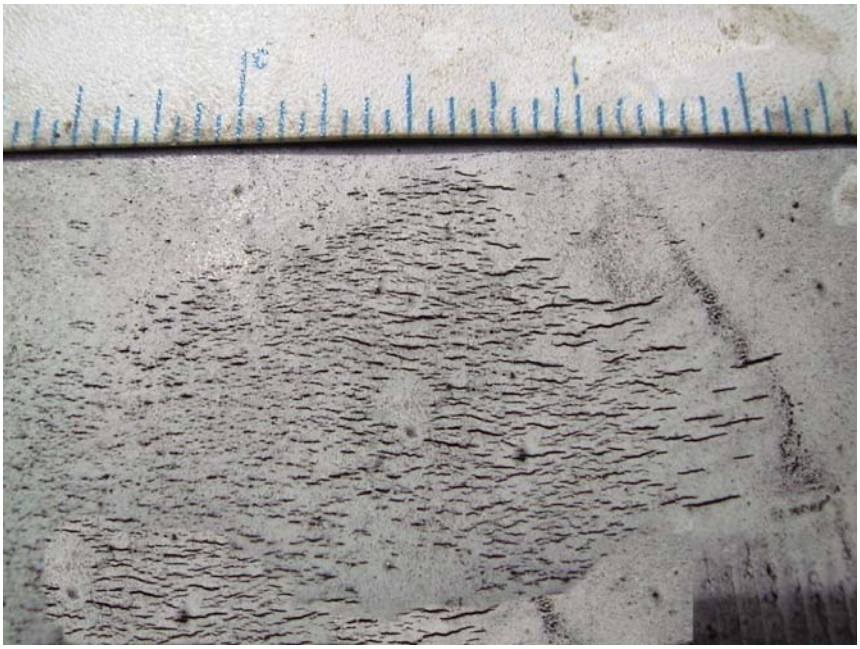

Figure 2 An SCC colony detected using MPI.

Once cracks have been detected, manual measurements of colony and crack dimensions (excluding depth) can be performed. Due to the sheer volume of cracks within a small area of affected pipe, these dimensional measurements are practically a best effort estimate. More recently, eddy current techniques have been introduced for detecting and imaging SCC. As discussed later, eddy current imaging was included in the demonstrations performed at the end of this project.

4.0 DEPTH MEASUREMENT OF SCC

4.1 Conventional Techniques

Various efforts have been made to measure SCC depth using transducer-based ultrasonics with varying degrees of success. The physical characteristics of SCC make it exceptionally hard to measure using *conventional shear-wave ultrasonic techniques*. Specifically:

- Irregular crack shape: Standard ultrasonic inspection techniques are based on calibrating the system using known, idealized reflectors and deducing results for real anomalies by comparative interpretation of the response. While this approach has been successful with simpler geometries, SCC, with its highly irregular shape and branching has been a challenge for conventional ultrasonics.
- Appearance of cracks in colonies: SCC occurs in colonies wherein individual cracks are closely spaced in generally similar direction. This makes it hard to identify and evaluate individual crack responses. Additionally, the couplant, needed for the ultrasound to enter the material, infiltrates into the cracks, effectively making the crack effectively invisible.
- SCC within corrosion: SCC, sometimes occurs within areas of general corrosion with highly irregular surface. This makes it harder for the transducers to couple with the pipe and for sound to travel through the pipe material.

Aside from conventional ultrasonics, a number of other techniques have been attempted. Efforts to implement electromagnetic techniques for sizing of SCC have generally shown some promise

in detection of SCC, but sizing has been a challenge due to the random geometries of cracks and their proximity within a cluster. Attempts have also been made to use EMAT transducers with in-line-inspection tools with limited results. Technologies such as ACFM and ACPD have been tested on SCC with some success, but have failed to provide a comprehensive solution.

4.2 Applus RTD study

In early 2005, Applus RTD initiated a joint industry project, "Parametric Study of Ultrasonic Techniques for Stress Corrosion Cracking" with the objective of improving the understanding of how various ultrasonic inspection techniques would perform at sizing SCC.

To do so, Applus RTD utilized a finite-difference based simulation technique in order to understand how sound interacts with the cracks as found in a stress corrosion colony, and to determine if any of the commonly used conventional ultrasonic techniques such as shear wave, time of flight diffraction (TOFD), crack tip diffraction, and phased array could be used reliably to determine the depth of the cracks as found in SCC.

The study revealed that while in some cases, one or more of the techniques may provide accurate depth measurements; the reliability of such measurements was very much a function of operator skill and experience as well as the distribution and characteristics of the cracks within a colony. The study also determined that TOFD was the most reliable and widely applicable technique for depth determination of cracks, if it could be ensured that the ultrasonic response would not be affected by the neighbouring cracks.

5.0 PURPOSE OF THIS PROJECT

The goal of the proposed project is to apply the proven technologies of laser ultrasonics and finite difference modeling to the important problem of depth measurement of stress corrosion cracks. Laser ultrasonics offers a number of significant benefits for the sizing of SCCs including small footprint on the pipe, rapid scanning and high bandwidth. Laser generation produces a rich admixture of ultrasonic waves, covering many wave types, directions and frequencies. Finite difference modeling offers a very promising pathway to harnessing these waves for effective crack depth measurement.

Our Work Plan covers a two-year effort that includes tasks on finite difference model development, laboratory optimization of the inspection process and development of a scanning prototype system to be used on pipes with known SCC.

The specific technical tasks are described below.

5.1 *Task 1*: Applying Finite Difference Model to Laser Generated Waves

The objective of this task is to model the ultrasonic waves generated by a laser at the surface of the material and subsequent propagation through the material to study the behavior of ultrasound generated by the laser and to use this information for performing targeted optimization in the laboratory.

5.2 *Task 2*: Laboratory Optimization of Laser Ultrasonic Screening and Sizing

Information provided by the finite difference calculations in Task 1 will be used to optimize the laser beam parameters and signal processing for optimum performance in the screening and the sizing modes.

5.3 *Task 3*: Development of System Specifications

The objective of this task is to establish the requirements and specifications for a prototype scanning tool that would implement the developed laser ultrasonic technique for scanning and measurement of SCC in the field.

5.4 *Task 4*: Design and Testing of the Prototype Laser Ultrasonic Inspection System

Based on the test conditions and measurement specifications determined in the Task 3, the scanning laser ultrasonic inspection system will be designed and constructed, followed by testing on SCC samples.

6.0 FINITE DIFFERENCE MODELLING

All wave phenomena obey one equation known as the wave equation. For wave phenomena in solids, the wave equation is usually referred to as elastic wave equation. This equation accounts for both shear and pressure waves. In addition, mode conversion and boundary waves (such as Rayleigh waves, love waves, creep waves etc.) are also accommodated.

A number of approaches are known for solving the elastic wave equation for given boundary conditions (geometry) and initial conditions (time signal). For this study of SCC, we have made use of a 2-D numerical model, the elastic finite difference model, which is superior to other methods such as ray tracing techniques or point source synthesis and is the discrete version of the wave equation on a fine grid. In this method, the motion of the wave away from the initial signal at a position of the grid is calculated at small time increments. The model is superior to other available methods since: (1) both pressure waves and shear waves are calculated, (2) mode conversion is calculated, (3) particle velocity, pressure and stresses are obtained separately (as opposed to other models, (4) energy profiles (or beam profiles) are obtained in relation with the geometry, (5) reflection at complex geometry is adequately addressed, and (6) the interaction of ultrasonic waves "trapped" between cracks in a cluster is calculated properly.

7.0 LASER ULTRASONIC TESTING

Laser ultrasonic testing is a modification of the conventional, transducer-based ultrasonic inspection. Conventional ultrasound uses piezoelectric crystals for generating and detecting ultrasound. Electrical pulses, when introduced into these crystals, cause the crystal to expand or contract. The characteristics of these oscillations, and subsequently produced sound waves can be controlled by controlling the electric pulse and its energy.

In laser ultrasonics (Figure 3), the ultrasound is generated by using a pulse laser. When the laser beam is incident on the material to be inspected, it generates ultrasonic waves in the sample. These waves then travel through the material and interrogate a certain feature in the material (such as a defect), as well as reflecting from the back wall. When the scattered or reflected wave returns to the surface, the resulting surface vibration is detected with a separate laser interferometer.

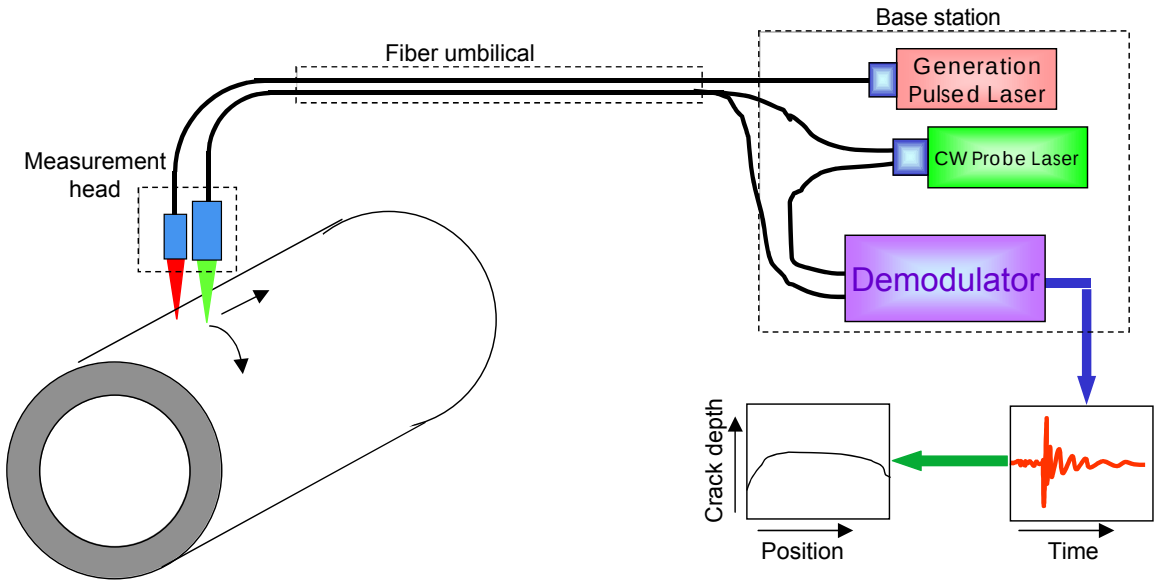

Figure 3 Basic laser ultrasonics setup.

In summary, laser ultrasonics has several advantages over other NDT techniques: (1) it is non-contact, with only laser beams reaching the pipe wall, (2) the small beam footprint provides access to the small spaces between cracks and allows generation and detection on corroded surfaces, (3) fast scanning is possible by motion of a scanning laser head, (4) all common ultrasonic waves can be produced, (5) the directional properties of the waves are well suited for implementation of TOFD and (6) the high bandwidth of laser-generated waves (typically 50 MHz) provides high resolution of crack depth and enhanced diffraction from the crack tip.

8.0 CRACK SIZING USING LASER ULTRASONICS

Two techniques for sizing individual cracks using laser ultrasonics have been studied in the past, and will be considered in this project. Each will be described separately below.

8.1 Time-of-Flight Diffraction (TOFD)

This approach has the advantage that the crack depth is determined from measurement of an arrival time, rather than signal amplitude. If longitudinal waves are used, the high velocity insures that the pulse arrival will precede all other arrivals. For shear waves, caution should be used in separating the desired arrival from other unimportant arrivals. TOFD using laser ultrasonics has some unique properties, compared with conventional approaches. First, we can choose to optimize shear waves or longitudinal waves (or both). Second, the large frequency range in the generated waves improves the likelihood of significant diffraction for a range of crack properties. Third, the crack is typically in the near field of the generated waves (at least at lower frequencies), so a geometric ray tracing approach to the problem is too simplistic. The proposed finite difference calculations will provide a more accurate picture of wave generation, propagation and diffraction at all frequencies.

Prior to the start of this project, Lasson Technologies, now part of IOS, performed a preliminary measurement of TOFD in a steel pipe sample with a series of EDM notches. We positioned each of the laser beams on opposite sides of the crack and at a separation from the notch that was equal to the notch depth, which was 1/8 inch (3 mm). This arrangement (Figure 4) is optimized

for waves that travel at 45 degrees to the surface normal. Scanning started on the clear area away from the notch and proceeded parallel to the notch until both the clear area and a portion of the notch were covered. Measurements of the temporal signal (surface displacement versus time) were made at equally spaced locations. As the scan passed over the simulated crack, the Rayleigh arrival disappeared and a new arrival appeared. The transit time of the new arrival is in agreement with the calculated time for a shear wave to travel from the point of generation to the bottom of the notch and then to diffract to the point of detection.

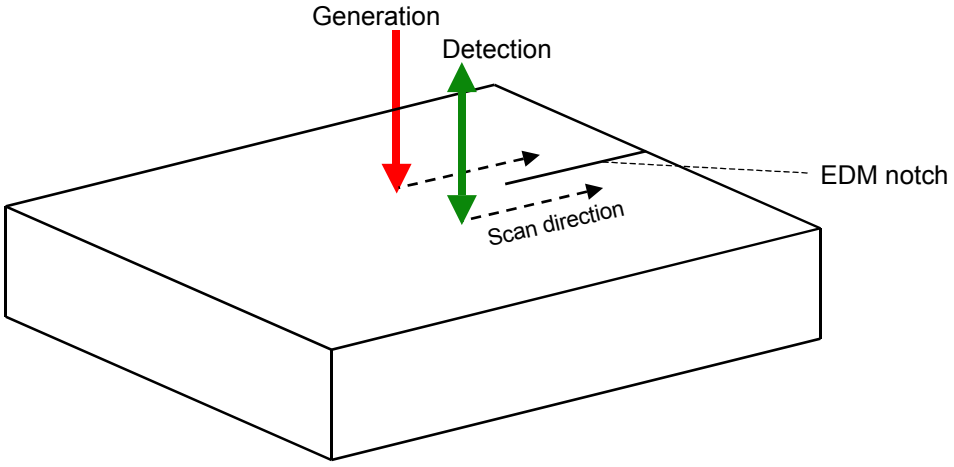

Figure 4 Scan pattern for EDM notch.

8.2 Rayleigh Wave Filtering.

For cracks that are not more than a few mm deep, a different phenomenon using the same straddling geometry as shown above, but involving Rayleigh waves can be considered. The wide bandwidth of laser-generated Rayleigh waves insures that there will also be a spread of wavelengths in the propagating pulse. It is well known that at any given frequency, Rayleigh waves penetrate only about one wavelength below the surface. When a broadband pulse encounters a crack, the shorter wavelength components will be nearly 100% reflected, while the longer wavelength components will partially pass under the crack and continue to propagate. In this way, the crack acts as a low-pass filter on the Rayleigh pulse. It is straightforward to quantify this filtering effect by measuring the bandwidth of the detected pulse over a clear area and over the notch, using the Fast Fourier Transform (FFT). The frequency cutoff for the crack-based filter is an indicator of the crack depth.

Lasson performed a preliminary measurement of Rayleigh filtering on an EDM notch that was 1/16 inch (1.5 mm) deep. As the scan passed over the notch, the Rayleigh arrival was slightly delayed and strongly broadened, due to the low-pass filtering action of the crack. Examination of the Rayleigh arrival in the frequency domain revealed elimination of the high frequency components over the crack.

9.0 RESULTS OF THIS PROJECT

9.1 *Task 1*: Applying Finite Difference Model to Laser Generated Waves

9.1.1 Knowledge Transfer

Coordination of efforts among the diverse performing organizations has been a critical requirement. In the first year of the project, the performing organizations were Lasson

Technologies (later sold to Intelligent Optical Systems), Applus RTD (Houston), Applus RTD bv (Rotterdam, Netherlands), and TNO (Delft, Netherlands). In order to optimize information transfer, a series of team coordination meetings took place at RTD bv on April 18-20, 2006. The agenda covered (1) project goals, (2) project schedule and milestones, (3) roles and responsibilities, (4) reporting requirements, (5) administration and finances and (6) action items. During a visit to TNO, there was a wide ranging discussion of their technical capabilities and the requirements for the finite difference simulations they will be performing. The action items that resulted from the meetings covered both technical and administrative topics. Since this meeting, there have been regular and frequent communications among the team members.

On May 24, 2006, Jim Merritt, the DOT technical monitor, visited Lasson for an informal kickoff meeting. Martin Fingerhut of Applus RTD was also present. The meeting agenda included a debriefing of the team proposal, a laboratory demonstration, a review of administrative issues and a discussion of near term technical objectives.

9.1.2 Simulation of the Laser Generation Process

The fundamental parameters in the 2-D finite difference simulations are the particle velocity perpendicular to the surface (Vz), the particle velocity parallel to the surface (Vz) as well as the stresses (normal Tzz, Txx and shear Txz). The results of the simulations can be displayed in a number of forms:

- Video clips with the Vz or Vx components
- Video clips with the Txx or Tzz or Txz components
- Video clips with the kinetic energy ($Vz^2 + Vx^2$) , in which the shear and compression components can than be illustrated in different colors
- Video clips with quiver plots showing direction arrows of particle velocities
- A-scans of the Vz, Vx component at the surface at certain positions. These are the quantities that can be observed and measured externally. Specifically the out-of-plane velocity Vz or the displacement Dz (time integral of Vz) are what would be measured by a laser ultrasonic receiver.
- Energy distribution plots. Three different energy distribution plots can be made, only the shear energy, only the compression energy or both.

The first step in the model development was to apply the finite difference approach to the laser generation process in the ablation regime (see plots in Figures 5 and 6). It is critical that the simulation results should reproduce analytical results in the scientific literature for laser generated waves. For these calculations the grid size was taken to be 1/10 of the shortest wavelength that is allowed by the model. In our case we have selected an upper frequency of 50 MHz. The corresponding ultrasonic wavelength is approximately 60 μm. Based on the above criterion, the grid size was selected to be 6.25 μm.

In Figure 5 we show a snapshot of the propagating waves at t=0.3 μs. The laser generation process started at the top center at t=0. In the ablation regime the initial condition is a Tzz step impulse with width 10 ns and a spot diameter of 30 μm. The parameter that is represented is Vz, with red indicating positive amplitude and blue indicating negative amplitude. We see a longitudinal wave and a shear wave (traveling at ~1/2 the longitudinal velocity), as expected. The effects at a later propagation time (1.49 μs) are shown in Figure 6. The longitudinal wave shows a clear peak in amplitude along the surface normal from the point of generation. The

shear wave has a very small amplitude on the surface normal; substantial energy remains even at an angle of ~80 degrees to the surface normal. Note that a Rayleigh wave is clearly seen near the surface, traveling with a velocity slightly slower than the shear velocity. Finally, the wave with the straight wavefront is a head wave.

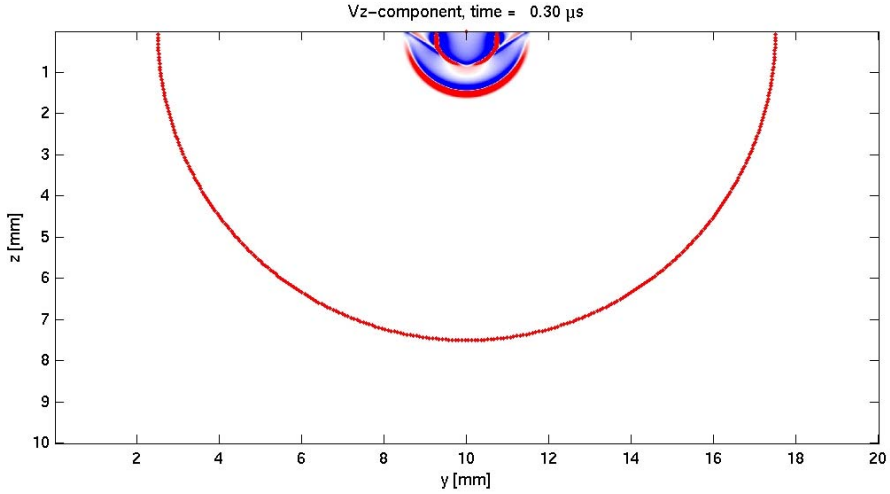

Figure 5 Propagating waves in the ablation regime at 0.30 µs after laser generation. The red semicircle is the locus of grid positions for the directivity plots in Figures 6 and 7.

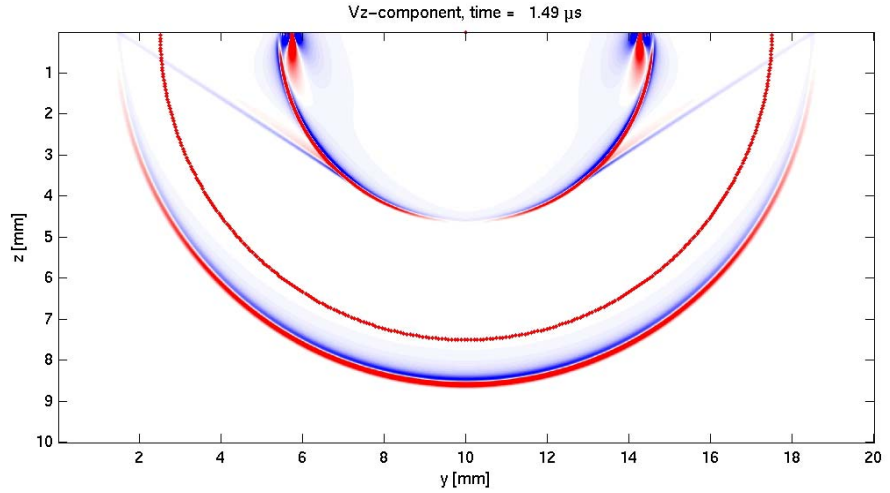

Figure 6 Propagating waves in the ablation regime at 1.49 µs after laser generation. The red semicircle is the locus of grid positions for the directivity plots in Figures 6 and 7.

Having calculated all components of the velocity and stress as a function of angle and time, we now wish to compare the wave directivity with analytical solutions from the scientific literature. In Figure 7 we plot the longitudinal wave (P-wave) amplitude as a function of angle from the surface normal. The simulation results are plotted in blue and the analytical solution is plotted in red. Similarly, in Figure 8 we plot the shear wave (S-wave) amplitude as a function of angle from the surface normal. In the case of P-waves, the agreement is excellent. For the S-waves the plots are close, with the remaining difference associated with the exclusion of head waves from the analytical model.

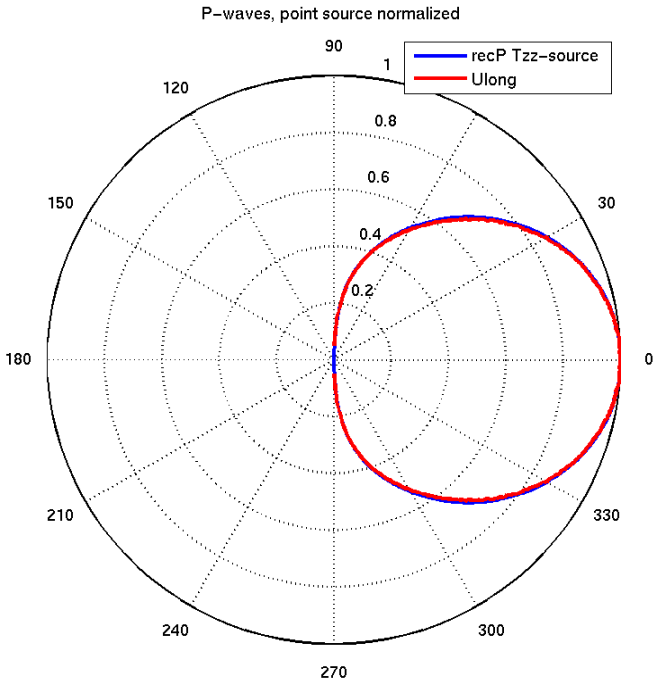

Figure 7 Plot of longitudinal wave directivity. The wave amplitudes were calculated at the grid points covered by the red semicircle at 7 mm radius shown in Figures 4 and 5.

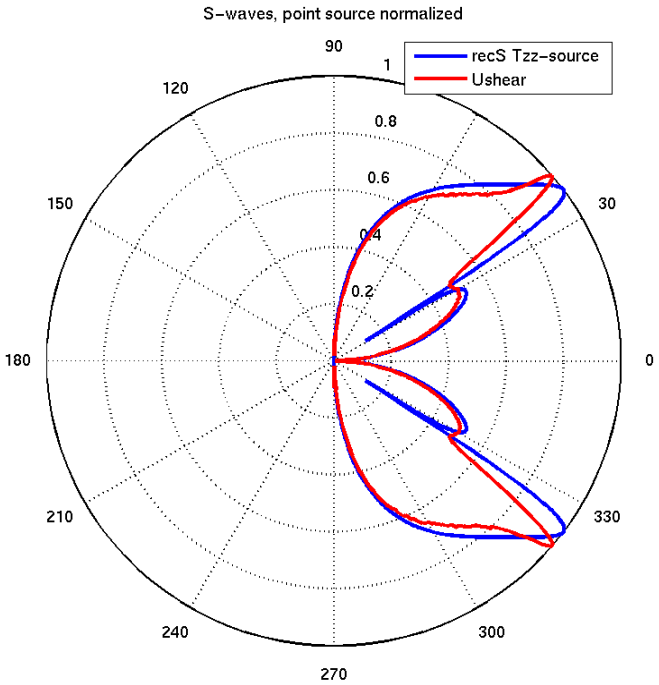

Figure 8 Plot of shear wave directivity. The wave amplitudes were calculated at the grid points covered by the red semicircle at 7 mm radius shown in Figures 4 and 5.

9.1.3 Simulations for Isolated Cracks

Using the laser generated waves modeled above, TNO and RTD bv extended the finite difference simulations to cover interaction of these waves with isolated cracks. The simulations have been completed. The results were prepared in a number of forms for each of the simulations in the table:

- Movie in the same view as Figures 4 and 5 showing propagation of all waves as they interact with the crack. Separate movies showing (1) the longitudinal and shear components and (2) the velocity in the direction normal to the surface were prepared. The movies give a very useful overview of the way all the waves interact with the crack.
- Wiggle plots showing the velocity Vz normal to the surface as a function of time, for a series of positions on the opposite side of the crack.
- Response plots which show the arrival time of the shear and longitudinal components as a function of separation from the point of generation.
- MatLab files of the solutions in each case which can be used to plot specific parameters not included in the above movies and plots.

In Figure 9 we show a frame (at 1.58 μs) of the longitudinal (P) and shear (S) waves propagating in a 5 mm thick sample with no crack. The waves were generated at position 1 mm in the figure. As in Figure 9, the main P wave in blue and the S wave in red are clearly seen as segments of circles originating at the point of generation. The head wave is faintly visible and the Rayleigh wave is seen clearly on the surface, just behind the shear wave. In this case of a finite plate thickness, wave reflections from the bottom surface (forming P and S waves) are seen. The presence of these and later reflections provides no information about the crack and is a potential source of clutter in the detected temporal signals from the top surface.

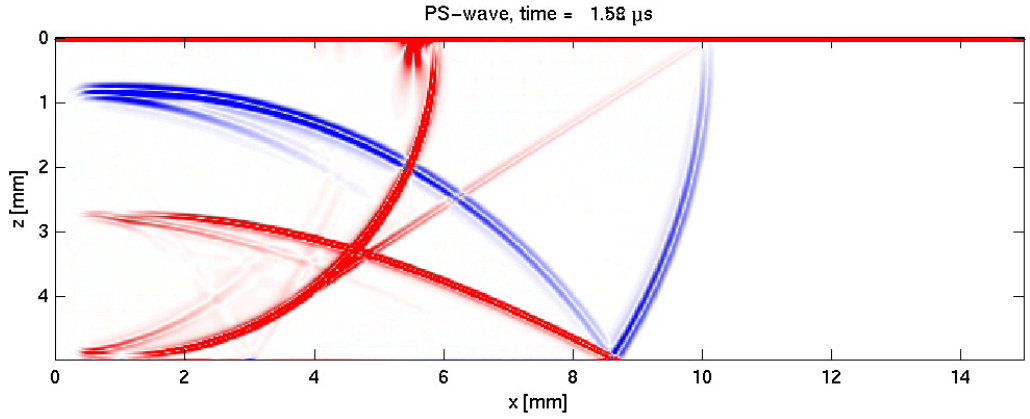

Figure 9 P waves (in blue) and S waves (in red) generated from a source at x=1 mm in a plate with 5 mm thickness.

As an example of simulation results showing wave interactions with an isolated crack, Figures 10 and 11 show frames of a movie showing Vz for the case where the crack is 1.5 mm deep and the source is 1 mm to the left. In Figure 10 the P and S waves have passed the crack tip and created diffracting waves shown in the two larger circles centered on the crack tip. The smaller circle is diffraction from a Rayleigh wave that traveled to the top of the crack and then propagated down to the tip. In Figure 11 the three diffracted waves have all reached the top

surface where they could be detected. In addition, there is a Rayleigh wave at x=5.5 mm that results from a Rayleigh wave that propagated from the source, down the crack, up the other side and then back onto the top surface. At later times there are many other bulk wave arrivals that are not useful for sizing the crack.

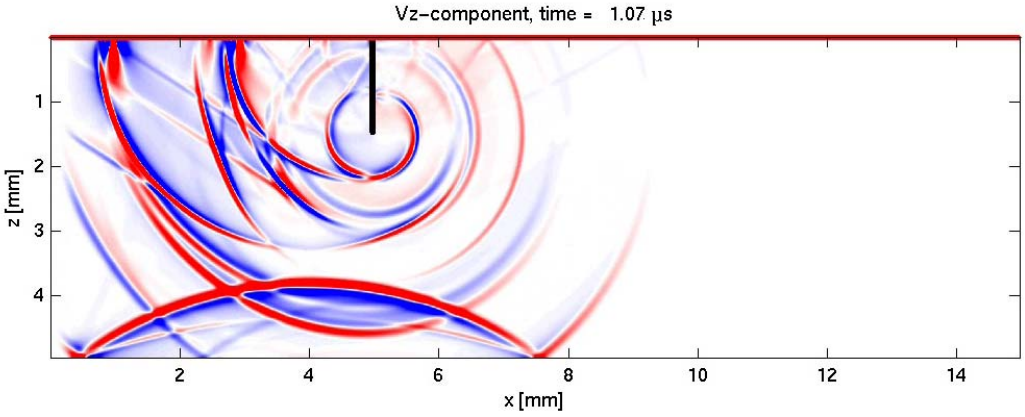

Figure 10 Frame at 1.07 µs of waves diffracting from a 1.5 mm crack positioned at x=5 mm. The waves are generated at x=4 mm.

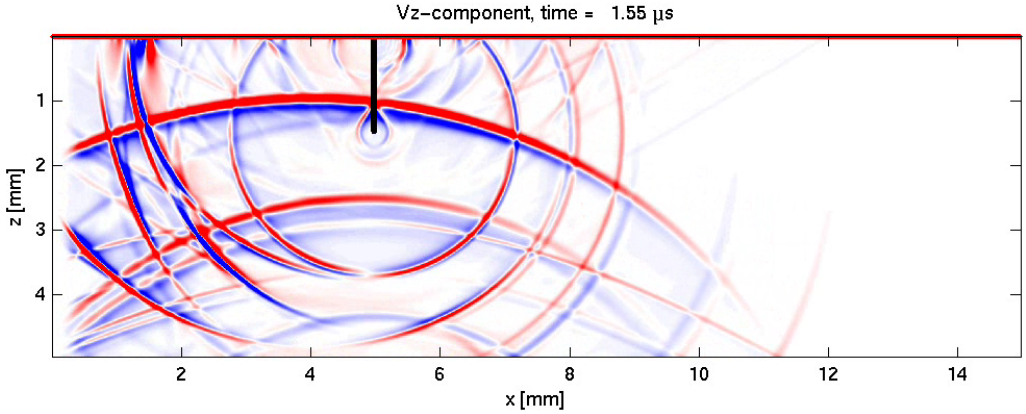

Figure 11 Frame at 1.55 µs of waves diffracting from a 1.5 mm crack positioned at x=5 mm. The waves are generated at x=4 mm.

The ultimate goal of the simulations is to determine the best position for detection, which provides high sensitivity to crack depth, while minimizing clutter from unimportant wave arrivals. When the beams straddle the crack, it is very difficult to separate arrivals in a single temporal signal (A-scan). The arrivals are associated with bulk waves reflected from the bottom surface, tip-diffracted bulk waves (shear and longitudinal) and Rayleigh waves created at the tip by mode conversion.

Rather than examining a single A-scan, it is much more useful to record A-scans for small increments in the position of the detection spot, starting on the same side of the crack as the generation spot, and then moving the detection spot toward a greater separation. The result is a separation B-scan, an example of which is plotted in Figure 12.

Figure 12 again shows the complexity of the arrivals. However, the information content is much greater than that in any single time trace. Specifically, the slope and origin of each arrival allows much more rapid identification. For example, any arrival that falls on a straight line can only be a Rayleigh wave or a head wave (surface-skimming longitudinal wave). The former have the steeper slope (slower velocity) and the latter have the shallower slope (higher velocity). The reason for the many separate Rayleigh arrivals is that Rayleigh waves are generated at the crack tip by mode conversion of each separate arriving wave.

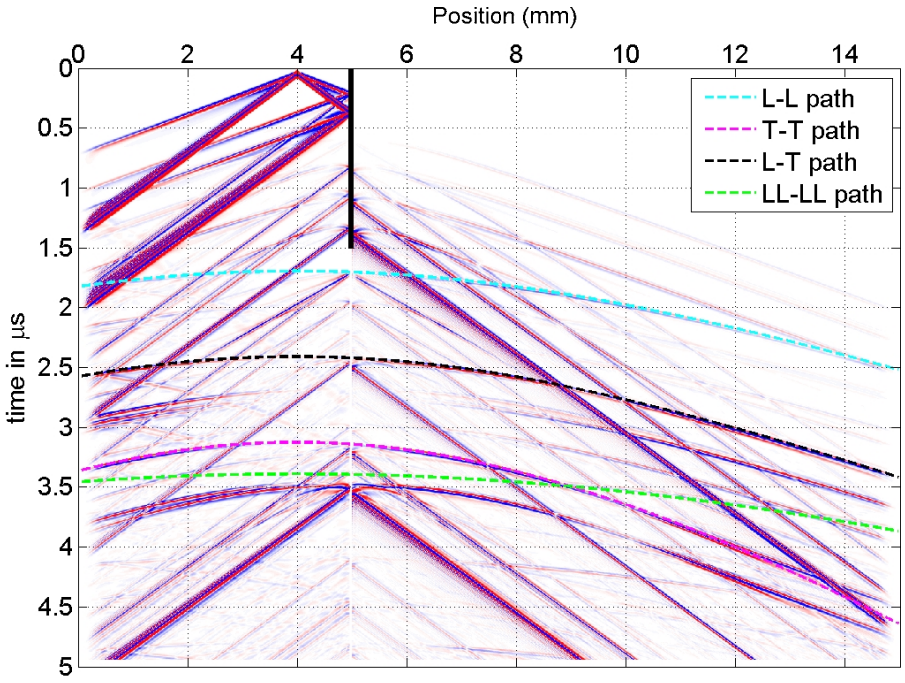

Figure 12 B-scan plot of the normal surface velocity as a function of detection spot position. The generation spot is at a position of 4 mm and the crack is at a position of 5 mm. The crack is 1.5 mm deep. Note that only the major bulk wave arrivals are labeled. Later plots will focus on the TOFD arrivals.

Any arrival that has a curved shape can only be a bulk wave reflected from the opposite face (identified in Figure 12) or a bulk wave diffracted from the crack tip. These waves can be readily distinguished by their curvature and arrival time.

Note also that the direct Rayleigh wave and surface skimming longitudinal wave (uppermost on the plot) are completely reflected by the crack. The lack of a transmitted direct Rayleigh wave is observed in all simulations and in lab data for all cracks 1.5 mm and deeper. This indicates that Rayleigh filtering will be limited in use only to cracks less than 1 mm deep and is thus of limited interest for this project.

9.1.4 Extension of Model to Complex Cracks

Unlike the EDM notches we modeled and tested, real SCC cracks have rough, uneven sides. They also curve and branch along their length. A typical SCC crack is shown in Figure 13 as a macro (left) and as modeled for the simulations in this task.

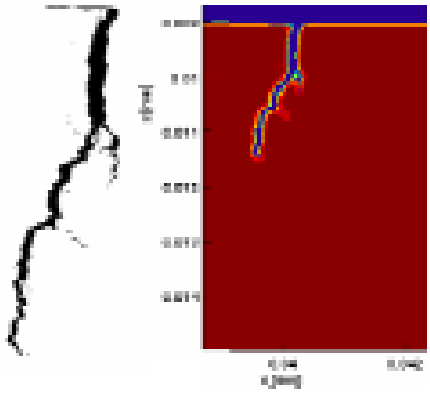

Figure 13 Typical SCC crack (left) and corresponding physical model (right).

As shown in Figure 14, the crack shown in Figure 13 and a second one were selected for the current simulations. The dimensions given in Figure 14 were measured on the real cracks. In order to allow comparison with previous simulations, the two cracks were scaled in depth such that the crack on the left was scaled in depth to 1mm and the crack on the right was scaled in depth to 2 mm.

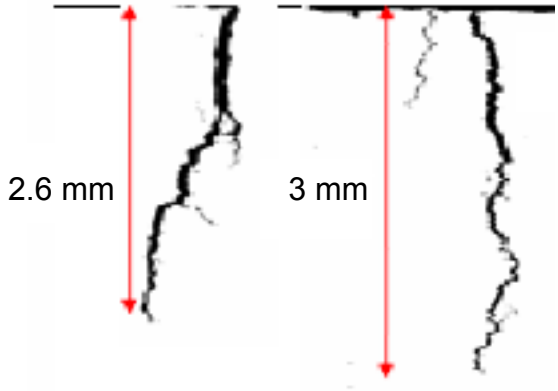

Figure 14 Two cracks used in current simulations.

A typical simulation B-scan is shown in Figure 15. The quantity plotted is the out of plane (z-direction) surface velocity, which is the quantity that would be measured in the lab. We see that there are a number of reflected Rayleigh waves that are associated with localized features on the side of the crack. However, on the far side of the crack, all diffracted arrivals are sensitive only to the tip of the crack. *The curved shape of the crack as a function of depth has no influence on the crack tip-diffracted waves*. One effect which is harder to observe is changes in the arrivals due to crack curvature in cross section. Plots like Figure 15 are based on distance from the top of the crack. If the crack is curved, the arrivals will shift in time. This effect is small at large distances from the crack, but it could be significant at close distances.

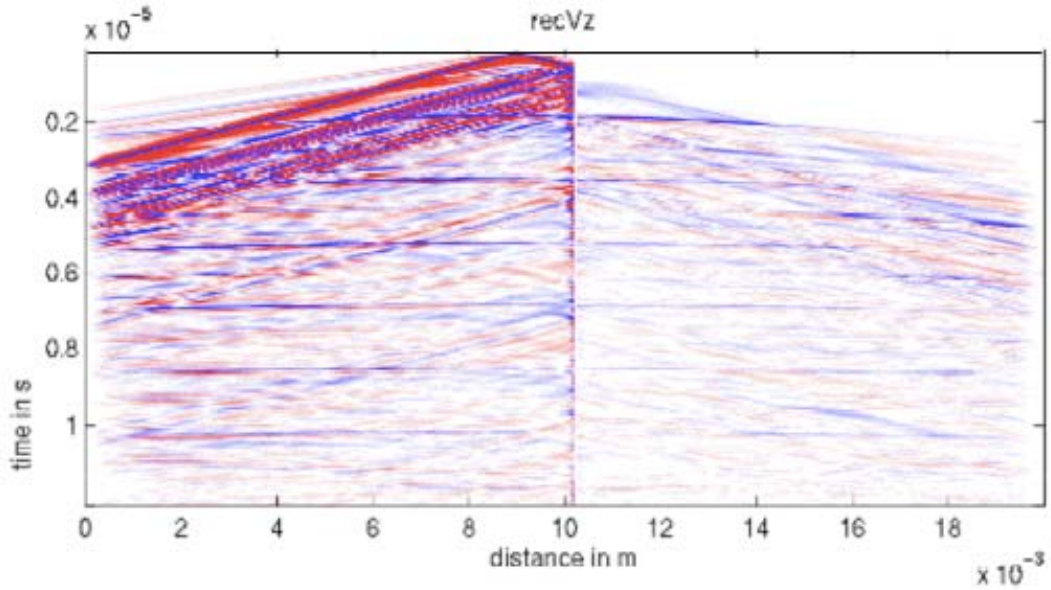

Figure 15 Simulated separation B-scan for a 2 mm crack, with the generation laser positioned 1 mm from the crack.

9.1.5 Extension of Model to Colonies of Cracks

The finite difference approach was applied to simulate the propagation of laser-generated waves across a colony of cracks. The specific configuration that we used for the simulation was a set of smooth, parallel cracks, each separated by 4 mm and varying in depth from 1 mm to 3 mm. A typical separation B-scan from this simulation is plotted in Figure 16. The generation laser is set 1 mm from the first crack. The detection beam is scanned all the way from 4 mm behind the point of generation to a position on the opposite side of the colony. By the time the detection beam is on the opposite side of the first crack (3 mm deep), no direct Rayleigh arrival is observed, which confirms our earlier observation that Rayleigh filtering is limited to shallow cracks. A weak TOFD arrival is seen on the opposite side, but no obvious TOFD arrival remains across the whole colony. In fact, there are only very weak ultrasonic arrivals on the far side of the colony. These results indicate clearly that no useful crack information can be obtained by straddling the whole colony.

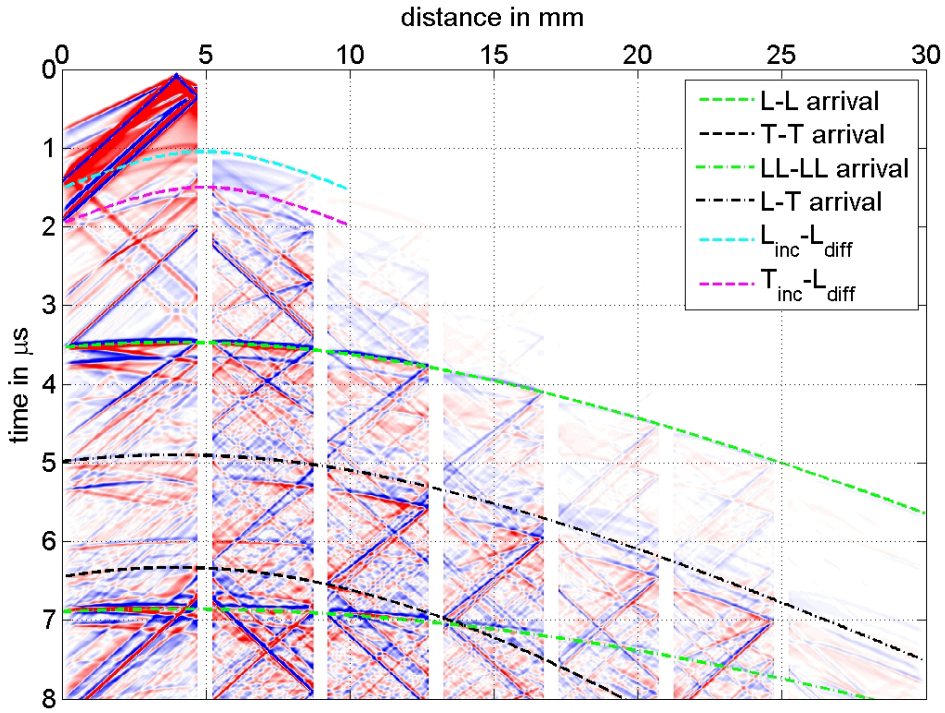

Figure 16 Calculated separation B-scan for colony of 6 cracks, starting at 5 mm and separated by 4 mm.

We also extended the simulations to include colonies of rough cracks. The crack model is shown in Figure 17. The crack morphology was obtained from a cross section of a real SCC colony. The simulations provided a separation B-scan in which the generation spot is 4 mm to the left of the far left crack and the detection spot is scanned across the whole colony. A typical simulated scan is shown in Figure 18. The survey scan on the left indicates that no tip-diffracted waves propagate as far as the opposite side of the colony. This result confirms earlier simulations on smooth cracks and once again indicates that straddling the whole colony would produce no useful information. The zoom scan on the right is more interesting. In spite of the neighboring crack (just off the figure on the right side), the Linc-Ldif arrival is free of any interfering arrivals. This arrival will always precede any other arrival and thus can be identified without ambiguity. This clear path to classification is a major benefit to the TOFD approach. By contrast, when the detection spot is on the same side of the crack as the generation spot, the crack tip diffracted arrival is still observed, but there is significant interference from the direct and reflected Rayleigh wave. The shock wave arrival (not shown) will add further interference.

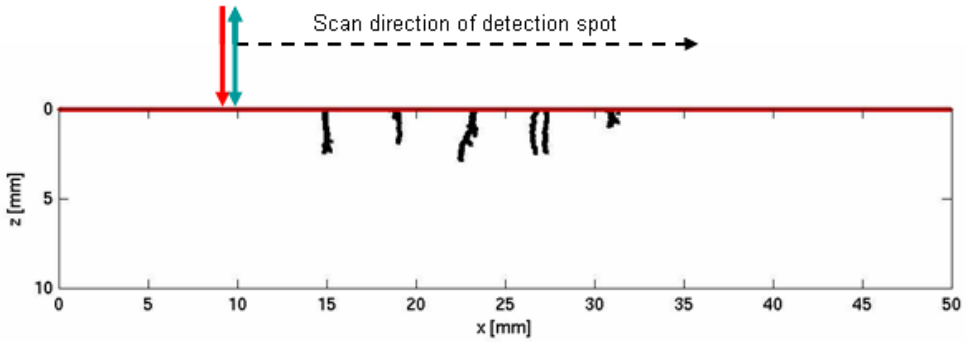

Figure 17 Physical model of a colony of rough cracks, showing the position of the generation and detection spots.

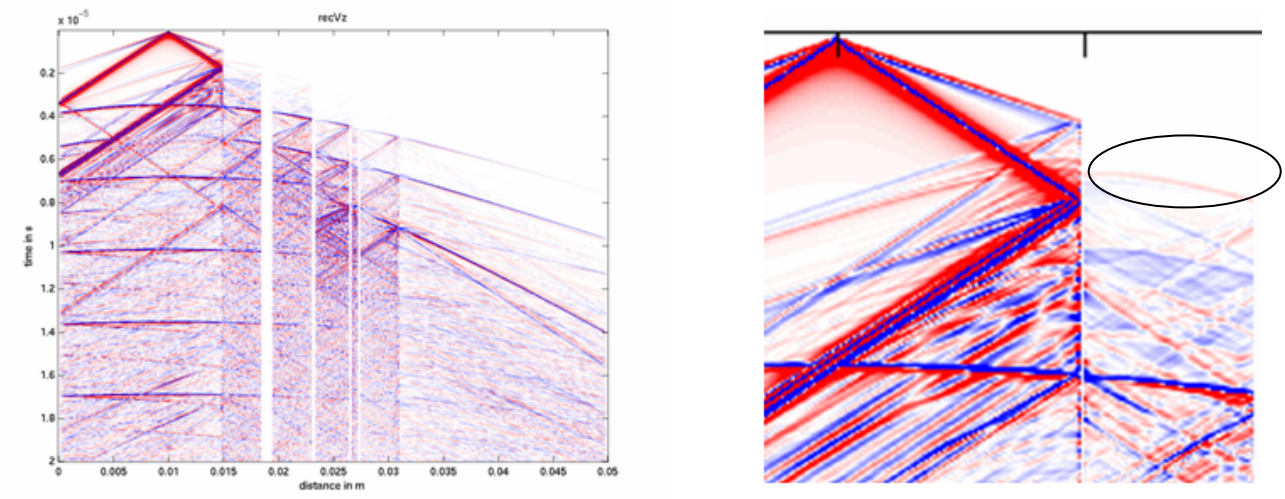

Figure 18 Separation B-scans across the colony shown in Figure 17. The scan on the left covers the whole colony. The scan on the right is a zoom on both sides of the nearest crack (upper left in the scan of the whole colony). The circled arrival is the Linc-Ldif (incident L-wave and diffracted L-wave) TOFD arrival.

9.2 *Task 2*: Laboratory Optimization of Laser Ultrasonic Screening and Sizing

9.2.1 Testing on Isolated Cracks

Our experiments were performed on test blocks with a series of EDM notches. The notch depths were 0.5, 1.0 and 2.0 mm. Plates with thickness 5 mm and 10 mm were fabricated and tested.

The measurements were made as separation B-scans, following the strategy explained earlier. For each measured scan, a simulation was run for the same physical conditions. Two examples of the plots that were generated are given in Figures 19 and 20. Note that in these plots the direct Rayleigh arrival is marked, along with waves that are mode converted at the crack tip into Rayleigh waves and into bulk waves. The back wall arrivals are also noted. The close agreement between the calculated and the measured arrivals gives us confidence that the simulations are functioning correctly.

For the case of a shallow crack (Figure 19), there is a strong direct Rayleigh arrival that could be used to obtain depth information by Rayleigh filtering. However, this same arrival is very low in amplitude for the 1.5 mm crack. This confirms our earlier assertion that the filtering effect is

only useful for shallow cracks. In addition, there are two other arrivals at nearly the same time that would make it difficult to process only the direct Rayleigh portion.

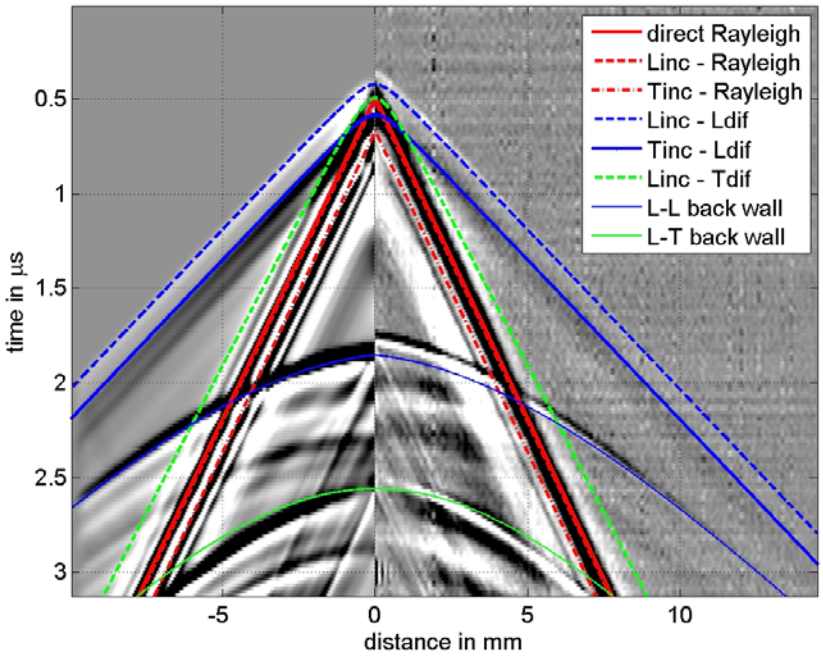

Figure 19 Separation B-scans for a crack depth of 0.5 mm, a generation position of 1 mm and a plate thickness of 5 mm. The left side shows the simulation and the right side plots lab data.

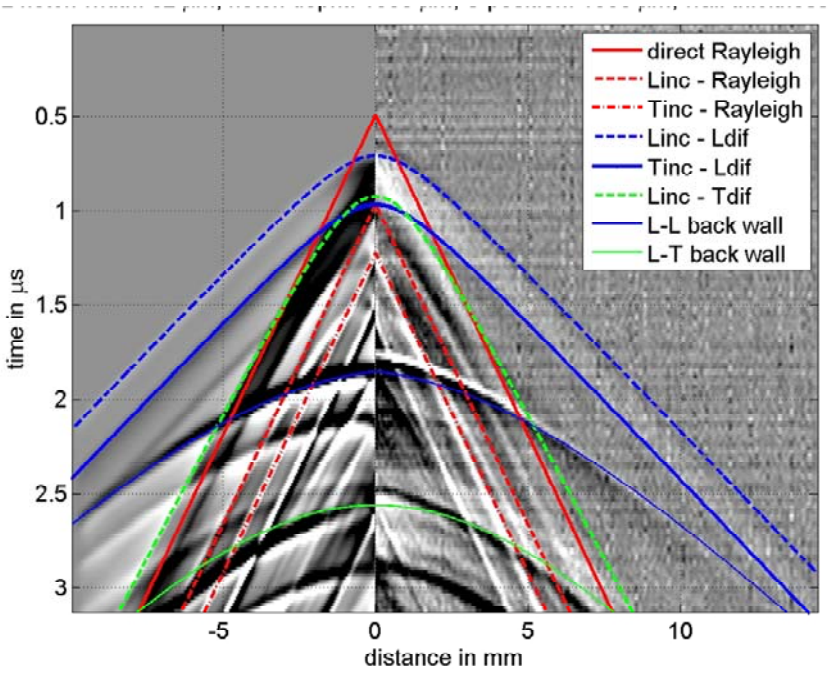

Figure 20 Separation B-scans for a crack depth of 1.5 mm, a generation position of 1 mm and a plate thickness of 5 mm. The left side shows the simulation and the right side plots lab data.

Using the B-scans shown above, we can anticipate two approaches to crack sizing. The first approach would do a fit of the simulation results to the data, with crack depth as a variable. This approach has the advantage of using all arrivals to enhance the measurement accuracy. However, it is computationally inefficient.

In the second approach, we would select one or two arrivals that are unambiguous in identity and have no interference from competing arrivals. The arrival time (at a given position) would then be used to determine the crack depth. In all our B-scans, the L-L and T-L crack diffracted signals (solid or dashed blue lines in Figures 19 and 20) arrive before most or all other arrivals. The signal amplitude of these TOFD arrivals is low in Figures 19 and 20 because the position of the generation spot is not optimum. When the generation spot is more correctly positioned, the TOFD arrivals are more easily observed.

9.2.2 Testing on Complex Cracks

It is clear from the above observations that the TOFD approach is preferred for depth profiling of cracks in a colony. The beam configuration for sizing top surface cracks is shown in Figure 21. The laser generation process produces bulk and surface waves. An incident bulk longitudinal wave is diffracted at the crack bottom to both a longitudinal and a shear wave, with the diffracted longitudinal wave generally being stronger. By detecting these waves and measuring their arrival time, the crack depth can be determined.

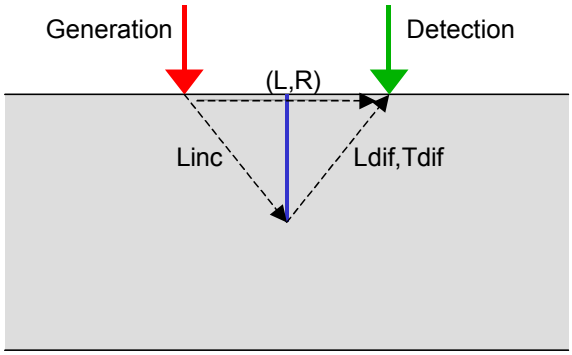

Figure 21 Beam configuration and propagating waves for TOFD. Linc is an incident longitudinal wave, Ldif is a crack-diffracted longitudinal wave and Tdif is a crack-diffracted shear wave.

We have performed several TOFD scans on cracks in an SCC pipe sample provided by Applus RTD. The sample (#10409) contained a high-pH colony over a large area. The wall thickness was 8 mm. Our measurements were made as straddle B-scans, as shown in Figure 21. A photo of a portion of the colony is given in Figure 22. A closeup photo of Crack B, showing both laser beams in position, is given in Figure 23.

Figure 22 Photo of a portion of the SCC colony in Sample 10409.

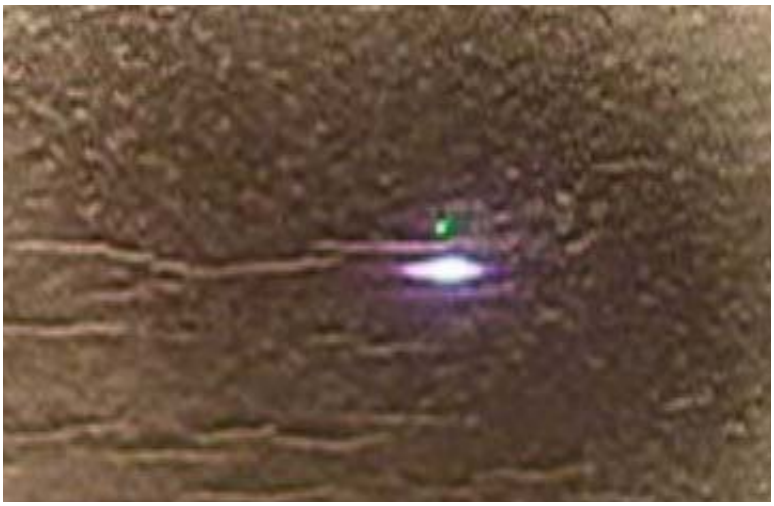

Figure 23 Close-up photo of Crack B shown in Figure 22. This image is the mirror of the one above.

In our experiments each beam was 4.2 mm from the crack. The beams were scanned together from right to left in Figure 22, starting off the crack and extending almost to the second neighboring crack. The resulting B-scan is shown in Figure 24. Two TOFD arrivals over the crack are noted: Linc-Ldif and Linc-Tdif. A strong direct Rayleigh arrival is observed before the beams straddle the crack. Using a geometric model and the measured arrival times of the diffracted waves, we were able to calculate the crack depth as a function of position along the crack. The data is plotted in Figure 25. We see that the crack starts with zero depth. At the end of the scan the depth is nearly 2 mm deep. This and other measurements have validated that the TOFD approach is a legitimate option for the requirements of this project.

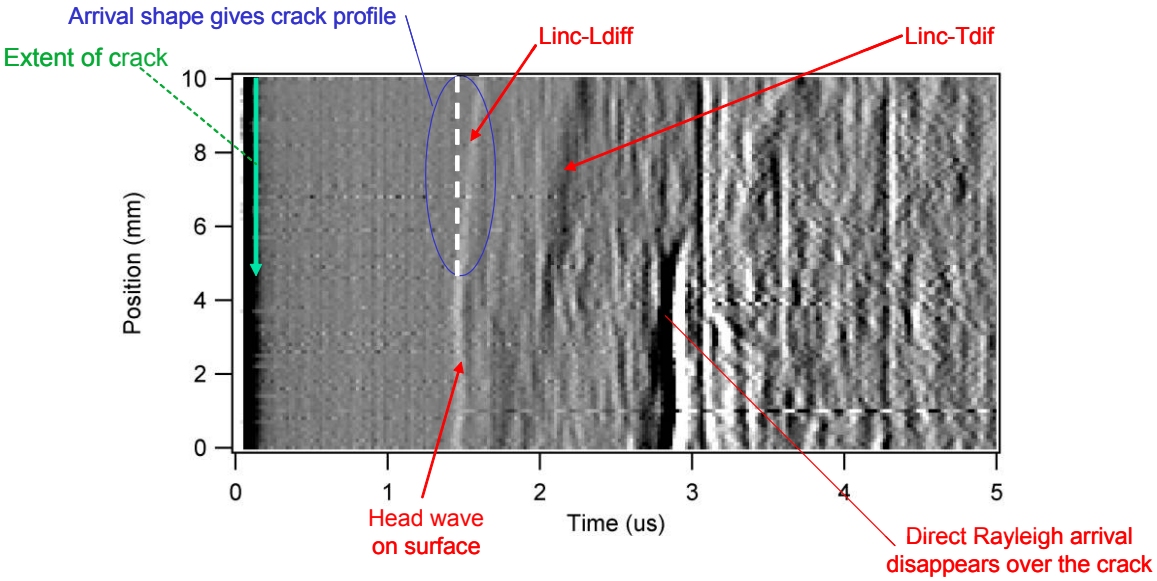

Figure 24 B-scan along Crack B.

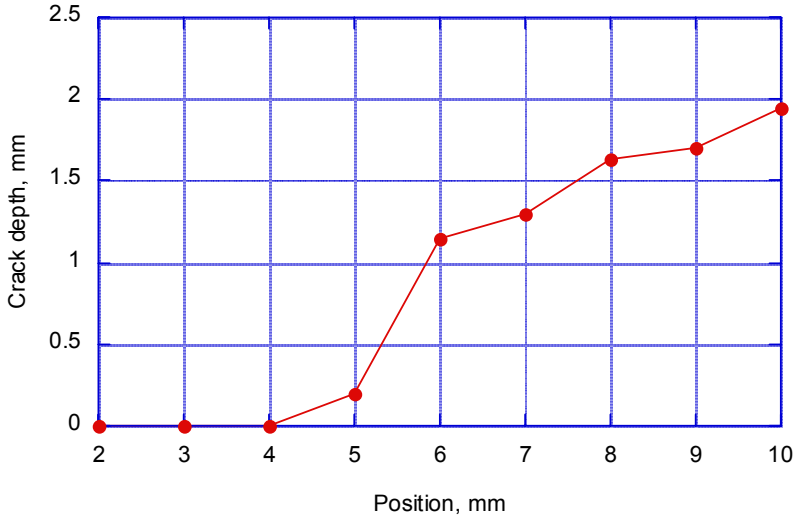

Figure 25 Measured crack depth vs. position.

9.2.3 Tolerance of TOFD Measurements to Crack Position

In analyzing the TOFD technique, it is important to understand the sensitivity of the diffracted wave arrival time to the depth and the lateral position of the crack. Ideally, the arrival time should be sensitive to the crack depth and insensitive to its lateral position. In Figure 26 we plot data intended to show the dependence of the TOFD arrivals on the lateral position of the crack. The minimum arrival time is in the symmetric configuration (a=c/2). As the crack position deviates from this configuration the arrival time increases. However, the increase in arrival time is modest over a significant range. A typical rate of change (slope) is 40 ns per mm of lateral shift. This low rate of change means that lateral shifts do not strongly affect the accuracy of depth measurement.

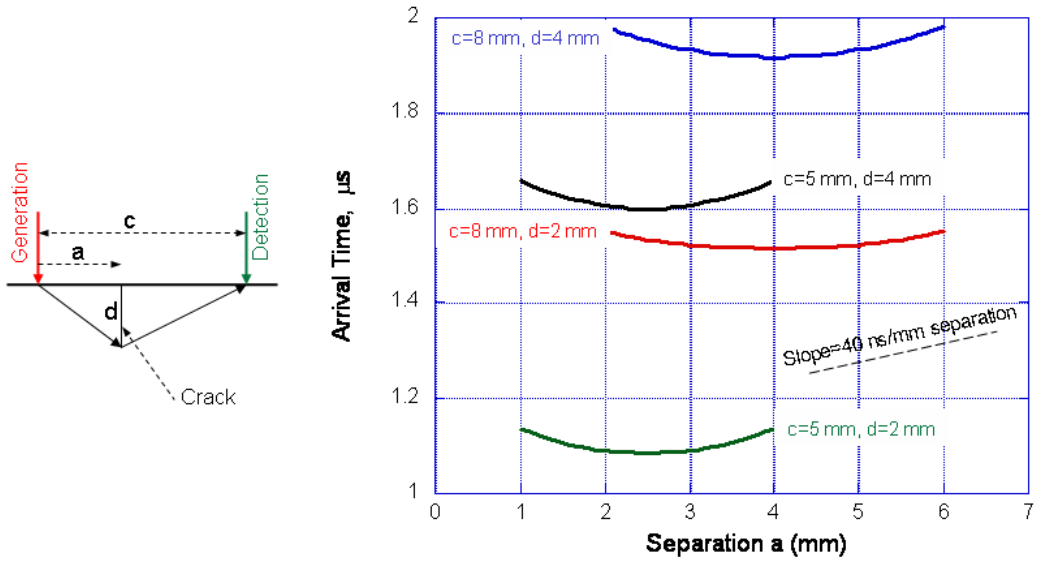

Figure 26 TOFD Linc-Ldif arrival time as a function of the generation distance a, for several values of beam spacing c and crack depth d.

9.2.4 Signal Processing Development

The goal of the signal processing development is to detect and classify the TOFD arrivals, measure the arrival time and then use this information to obtain the crack depth. Our processing approach uses wavelet processing. The wavelet transform is a convenient tool for decomposing a transient signal into a set of wave functions that consist of short bursts. Each wave function has a coefficient that determines its energy content. The coefficients are ranked in order of their value. Starting with signals for which the TOFD arrivals are identified, the coefficients not associated with these arrivals are zeroed out. The coefficients with the smallest values are associated with noise and are also zeroed out. The remaining coefficients are used to transform back into the time domain, with the TOFD arrivals identified. A correlation approach is then used to measure the arrival time and then trigonometric relationships are used to obtain the crack depth.

Based on the principles given above, we developed off-line algorithms to automate the described processes. An example of crack depth data obtained with our processing algorithms is given in Figure 27. The crack is a real SCC that had been scanned earlier. The blue and red lines were obtained from the raw scan data using our algorithms. There is very good agreement with depth values obtained by visual interpretation of the data.

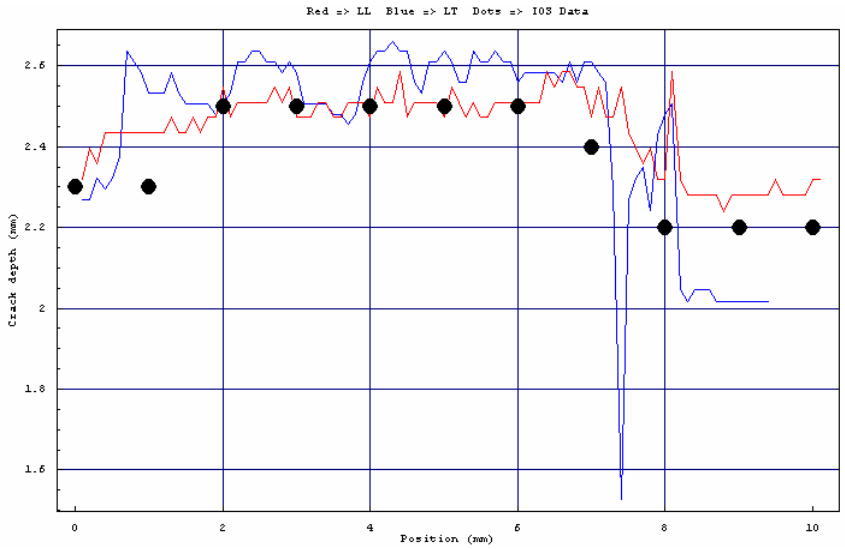

Figure 27 Plot of measured crack depth as a function of position along the crack, using offline software developed for this project. The red solid line is based on the Linc-Ldif arrival and the blue solid line is based on the Linc-Tdif arrival. The black dots are from a visual interpretation of the raw data.

9.3 *Task 3*: Development of System Specifications

9.3.1 Scan Requirements

On March 5-6, 2007 a program review was held at IOS. One objective was to develop the performance requirements for a full system. The nominal requirements were determined to be: (1) measurements are required every millimeter along each crack; (2) the scans should be able to cover 100 millimeters in 100 seconds. As a result, the required generation laser repetition rate is 1 Hz. However, the use of a 20 Hz laser will allow 20 averages with no loss in spatial resolution.

9.3.2 Practical Pipeline Inspection Requirements

In order for a system to be practical in the field, it is imperative that it be economical, reliable, rugged and foolproof. Based on the results from the first year of the project, it was determined that performing a raster scan on the entire pipe section would prove to be too time consuming and hence not economical. Therefore, it was determined that significant savings in scan time could be achieved by using an external tool for detection and mapping of SCC, with sizing performed on select sections of a colony corresponding to the 'significant cracks', identified by an analysis of crack locations, extent and dimensions within a colony. Time of flight diffraction using laser ultrasonics is ideally suited for this latter measurement.

Applus RTD has been involved in the development and validation of another technology, an eddy current based sensor technology, capable of detecting and providing a spatially accurate 2-D (top view) map of an SCC colony. Tests were performed using these sensors and results were verified as part of a joint industry project (JIP) funded by a few major North American pipeline operators. The findings from this JIP were used to determine the feasibility of this approach. It was determined that the data from the eddy current sensors could be reliably used to determine the locations of the various cracks within the colony.

A study of relevant literature revealed that various models are available in industry to identify the so called "significant cracks". Most such models use the measurements such as the axial and

circumferential separation between the cracks to determine the possibility of coalescence and therefore, identifying the cracks that could prove detrimental to the pipe, given a particular depth. It was determined that these models could be applied to the maps as obtained from the eddy current sensors in an automated fashion and the resultant "significant cracks" could be sized using laser ultrasonics.

9.3.3 Mechanical and Controls Conceptual Design

While simple in concept, one of the critical requirements of this process is that in order to get a good signal-to-noise ratio, the generation and detection lasers should be placed within an optimal range of distance from the crack(s). To ensure this, it is important that there is a common datum (reference point for measurements) for both the eddy current scan and the laser ultrasonics scan. The required precision in location of the laser beams makes it impractical to use two separate systems due to the lack of an external reference. *Therefore, it was determined that a setup has to be used that deploys both tools using the same platform.*

To satisfy this requirement, we have decided to use a band scanner used for automated weld inspection that can be adapted for use on this project (Figure 28). The scanner would be capable of moving the sensors in both axial and circumferential direction on the pipe. The sensor attachment would hold the eddy current sensor as well as the laser delivery mechanism.

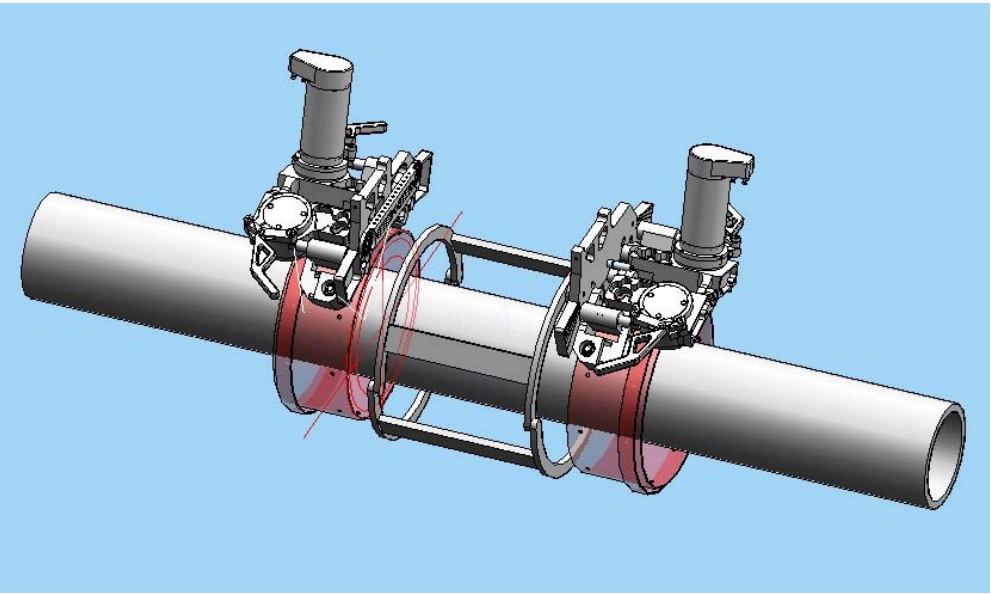

Figure 28 Schematic of the band scanner.

The benefit of using such a configuration is that it eliminates the need for an external reference as the setup doesn't move between successive inspections using different technologies. On the other hand, it does require moving the setup when moving along the pipe. Various configurable scanner systems are available in the market that can be considered for the application.

The eddy current sensor is a commercial device that can be easily modified to be affixed on to the sensor holders. The position data is recorded by inbuilt sensors in the scanner apparatus. The two can be combined to form a map of the SCC found within the scanned area (Figure 29).

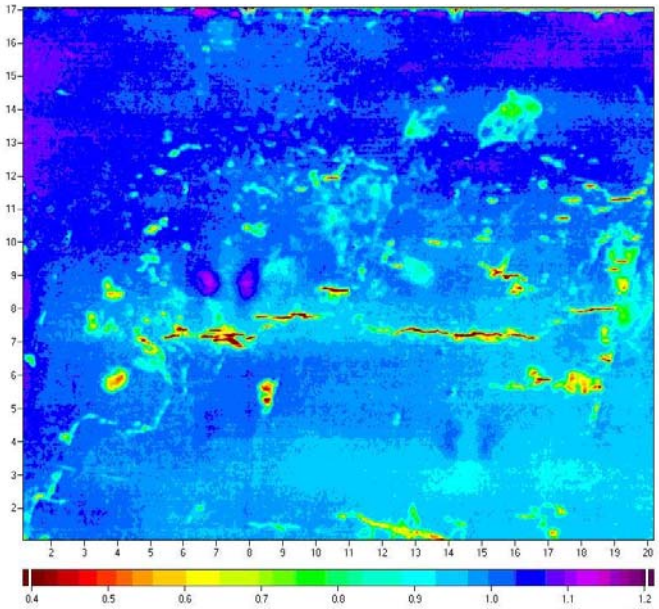

Figure 29 Example of a 2-D map of SCC colony as provided by the eddy current sensors.

After the data is recorded, it can be processed in almost real time to obtain the location and extent of the areas where sizing needs to be performed. Since the system hasn't moved, the actuators can easily place the laser beams at the determined locations and drive them along the cracks in 1 mm increments to obtain depth measurements.

9.3.4 Laser Ultrasonic Subsystem

The specific beam layout on the pipe surface is given in Figure 30. The generation spot should be rectangular, with a width of about 300 μm and a length of about 2 mm. These specifications were determined in the experiments performed in previous quarters. The detection beam can be circular, with a diameter up to about 300 μm. The beams will be positioned to straddle the crack being measured, with a spacing of about 4 mm.

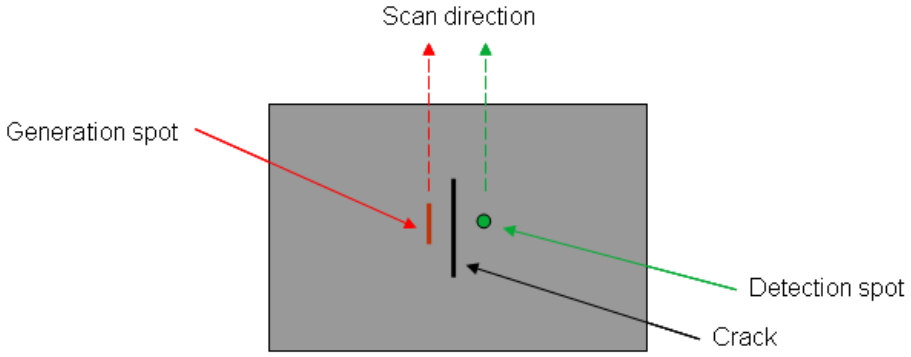

Figure 30 Optimized beam configuration on surface of pipe.

It is important to be able to deliver the generation laser pulses with sufficient energy to ensure good signal-to-noise in the measurement. This delivery should be through a fiber, to ensure that the measurement probe stays small. This fiber delivery is a significant challenge, because high energy pulses can cause permanent damage to the fibers. We have devised a delivery scheme that mitigates the fiber damage risk and also helps to shape the beam that is imaged onto the pipe

surface. This scheme is shown in Figure 31. The output beam from the pulsed laser is split into a number of beams (five in Figure 31) of equal pulse energy. To accomplish equal energy distribution in the five beams, the beamsplitter cubes have different reflectivities, ranging from 20% in the first channel to 100% in the fifth channel. Each beam is coupled into its own fiber. The reduced pulse energy in each fiber is now below the damage threshold. The fibers are joined together into a single fiber bundle organized into a linear pattern. The linear array at the bundle exit is then imaged onto the surface of the pipe to form a "line" similar to that shown in Figure 30.

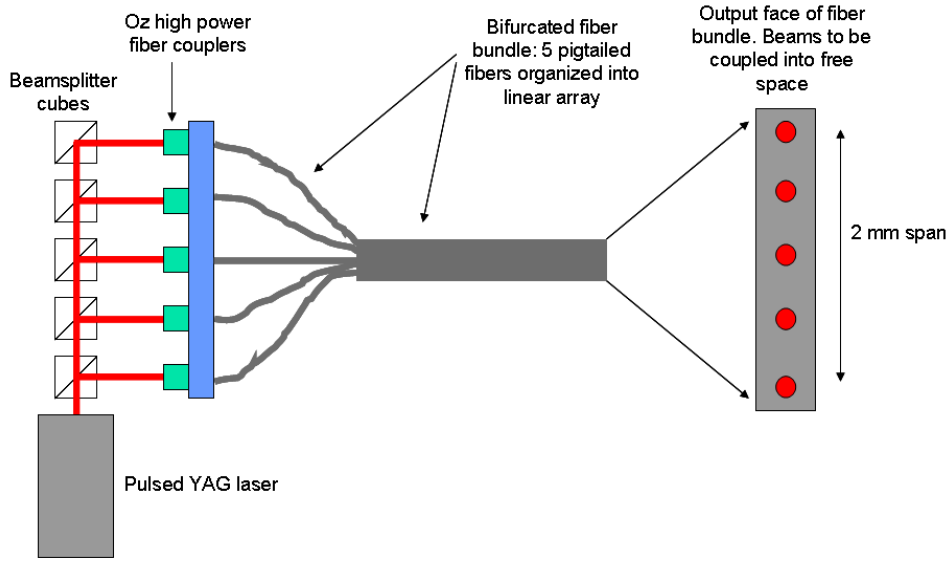

Figure 31 Laser coupling and fiber delivery scheme for the generation beam.

The subsystem at the left in Figure 31 is used to couple the generation laser into the 5 fibers. A photo of this generation module is shown in Figure 32.

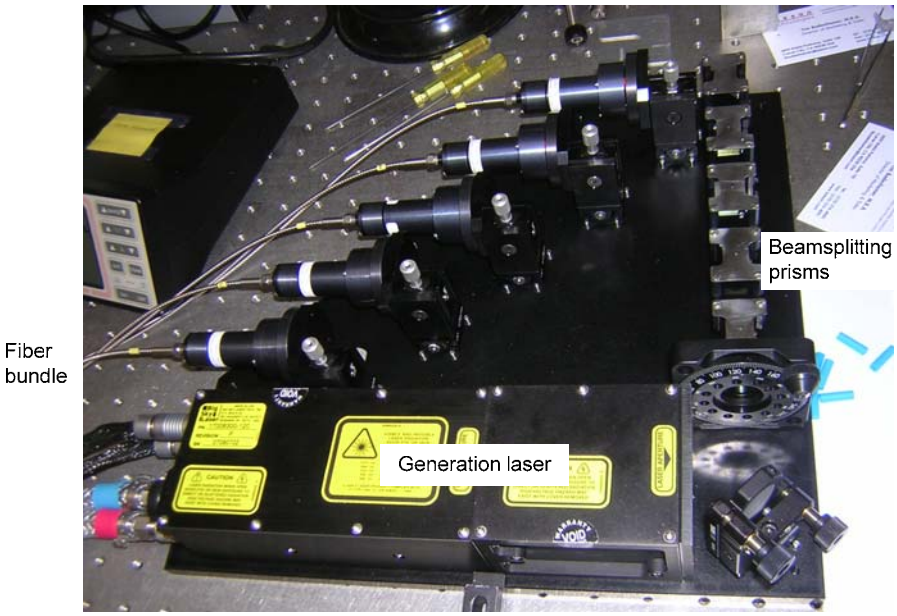

Figure 32 Generation module. The beam from the laser at the bottom is split into 5 beams and coupled into 5 fibers that are joined at their other end into a linear array.

9.3.5 Complete System Specifications

The desired system would ideally comprise the stationary, Z-θ scanner described above fitted with a platform that would hold the eddy current sensor as well as the laser ultrasonics laser delivery head. It is desirable that the rail would be flexible and will conform to various diameters of pipe. The scanner apparatus would allow both axial and circumferential movement of the sensor attachment. The sensor attachment may have an actuator to adjust the depth of field or a mechanical wheel attachment to maintain a reasonable standoff.

The data would be acquired, transmitted through an umbilical and processed using hardware housed in a protected environment. The scan parameters will be controlled by an operator remotely.

Once the scan parameters are entered, the system would perform a rapid scan of the area of interest using the eddy current sensor. The data thus obtained would provide a two dimensional map of the SCC colonies as found within the scanned region. Image processing techniques will be applied to this map to obtain the various measurements required to determine the location and extent of the "significant crack(s)". These values will then be fed back to the control system which will then guide the laser delivery heads to the appropriate location in the correct orientation. The system would then collect the data as obtained using laser ultrasonics and process it to obtain a depth profile for the "significant crack(s)".

The output from the system would comprise (in order):

- A 2-dimensional map of the SCC as found describing its location with respect to the pipe
- Highlighted "significant crack(s)
- A depth profile along the length of the "significant crack(s)"
- Evaluation results (not part of the scope for this project) using models such as NG-18 or CORLAS

9.4 *Task 4*: Design and Testing of the Prototype Laser Ultrasonic Inspection System

9.4.1 System Function

A drawing of the hardware layout for the IOS laser ultrasonic system is provided in Figure 33. This system has a number of unique and beneficial features. Most importantly, it is one of the first to deliver the high-energy generation laser pulses through an optical fiber. This capability is critical to the development of a field-ready system. It is not difficult to deliver the low power probe and signal beams through fibers, but the high energy pulses in the generation beam can cause optical damage at the fiber entrance face. Second, the measurement head uses a common aperture, i.e. both the detection and generation beams are emitted through the same objective lens.

A functional block diagram of the system is shown in Figure 34. The generation module was described earlier in this report. The measurement head is described in the next section. Prior to scanning a crack, the scanner moves the measurement head to a region on the pipe known to be free of cracks. The LaserScan software then acquires an averaged time trace at this one position that allows a measurement of the beam separation and that records the shape of the expected crack signal. This trace is an exemplar that is used later for cross correlation with the crack signals.

Next, the scanning controller moves the head to one end of a crack of interest and starts scanning, while sending a bit to the LaserScan acquisition software to start data acquisition. A second bit stops the acquisition. The data is then stored and displayed as a B-scan. The stored scan data, as well as the exemplar data and a parameter file are then loaded into a separate Mathematica Notebook, which is run to produce the desired plot of crack depth vs. position along the crack.

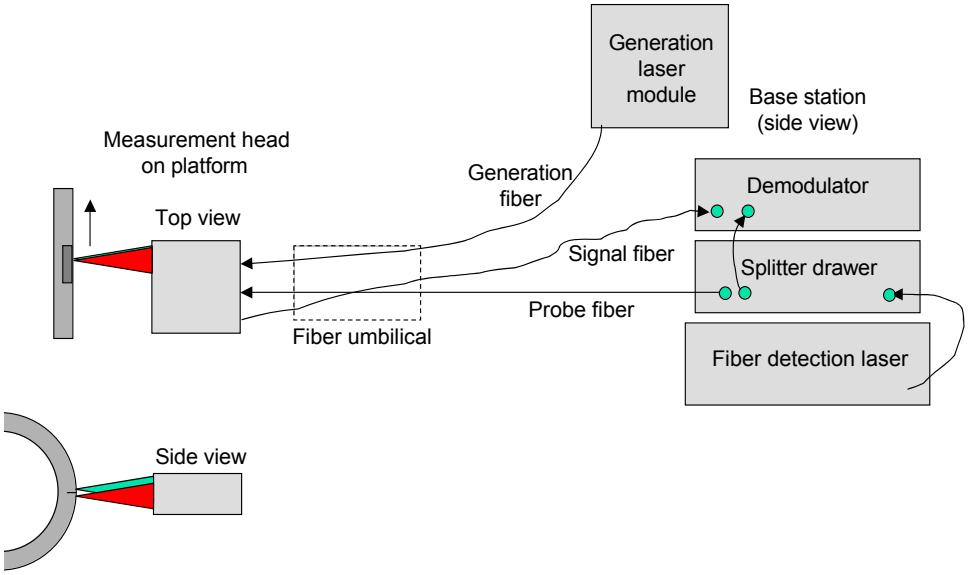

Figure 33 Laser ultrasonic system hardware.

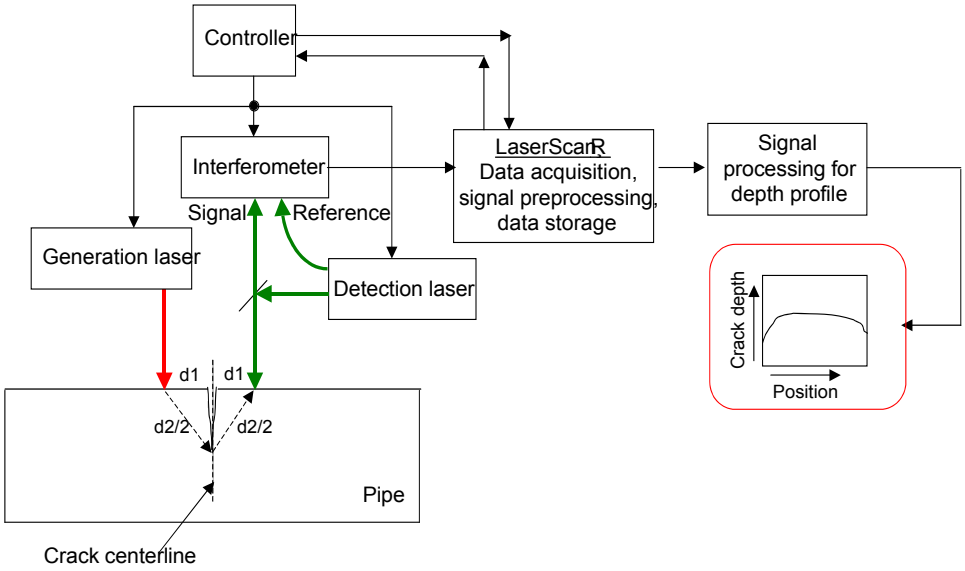

Figure 34 Laser ultrasonic system block diagram showing component functions. The colored lines represent optical beams.

9.4.2 Laser Ultrasonic Measurement Head

For this project, the critical element is the laser ultrasonic measurement head. The measurement head must be small and rugged, and must be able to focus the generation beam and the probe beam onto the pipe surface with a specific shape and size, and also with a known separation.

The head design uses a *common aperture* optical system. In this case, both beams exit collinearly through the same aperture; there is no beam spacing sensitivity to standoff; and the mechanical design is simpler. A schematic of our new design is shown in Figure 35. The probe and generation beams enter separate ports. They are combined at a dichroic reflector/mirror, and are directed through the same objective lens to the pipe surface (target). The collected signal beam passes through the system and is directed out of another port. The only critical optical component is the dichroic reflector.

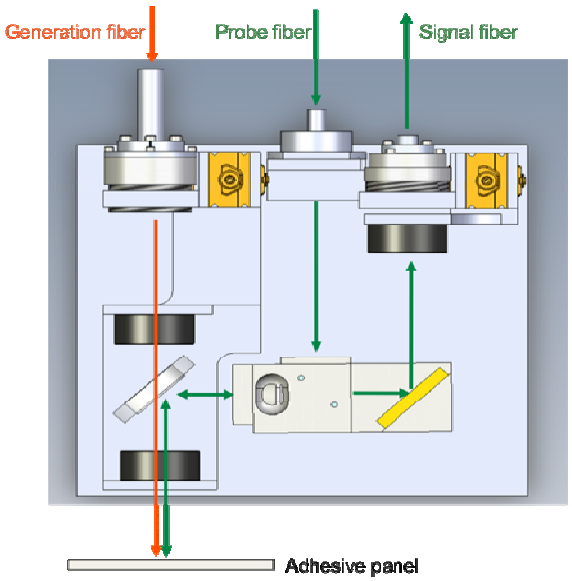

Figure 35 Schematic inside view of measurement head with optical layout.

A photo of the interior of the measurement head is shown in Figure 36.

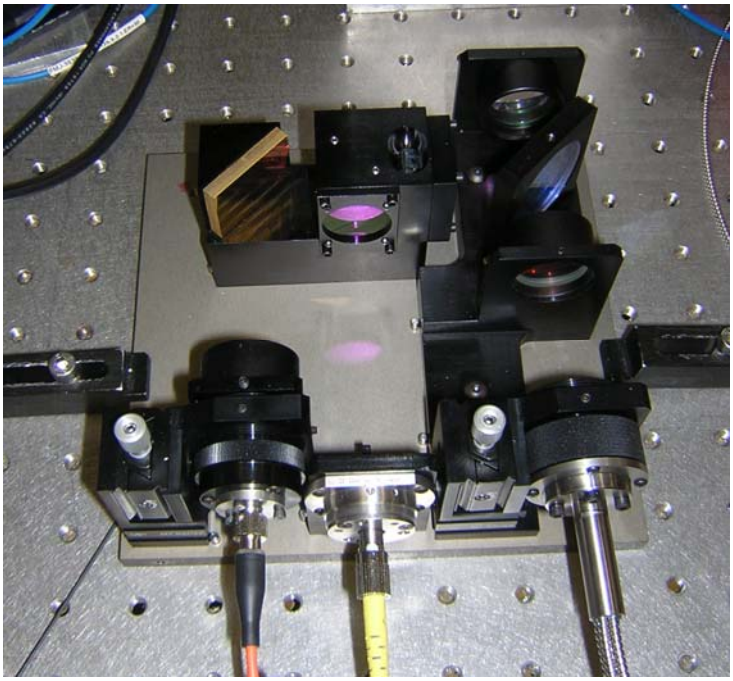

Figure 36 Photo of interior of the measurement head. The generation fiber enters at the right, the probe beam enters at the center and the signal beam exits on the left.

9.4.3 Generation Module Performance

The risk of optical damage at the entrance to delivery fibers is well known. Since the optical damage is fluence-related (with a threshold around 50 J/cm2), at a fixed pulse energy it is critical to use a large core multimode fiber and to expand the beam as much as possible at the entrance to this fiber. However, the use of a large core diameter reduces the spatial coherence of the beam that exits the fiber and makes it harder to focus this beam onto the target to a small enough spot size and with a reasonable depth of focus. For example, if we wish to deliver 50 mJ to the target, the fiber core diameter must be near 1 mm to avoid damage. In fact, Quantel Big Sky offers a fiber delivery option for their 50 mJ Ultra laser that uses a 1 mm core. In order to avoid the use of such a large core we designed our generation module (Section 9.3.4) to divide the 50 mJ beam into five beams and to couple each of these beams into five 400 um core fibers. We designed a fiber bundle that would combine these five fibers at the opposite end and organize them into a linear array of five closely-spaced spots. These spots would form a pseudo line focus that is known to be effective in coupling to the desired surface waves.

Using custom-designed fiber couplers prior to the demonstrations we performed damage measurements in 365 um and 400 um patch cables by gradually increasing the pulse energy until damage was observed. There are rather large statistical variations, but we observed that we could couple 10-15 mJ into such fibers before damage occurred. Therefore, we expected that an array of five of these fibers would be able to deliver 50 mJ to the target. However, we observed during the demos that the apparent damage threshold was much lower than 10-15 mJ and in fact was perhaps 5-8 mJ. Thus we were able to deliver only about 25 mJ to the target.

9.4.4 Receiver Performance

Our AIR-1550-TWM demodulator functions with the highest signal-to-noise when approximately 0.1-1 mW of collected signal light is directed to the photodetector. For rough target surfaces, more probe laser power is required than for smooth surfaces. The pipe surface at RTD was sandblasted to clean the surface, but the resulting finish was quite diffuse. We quickly determined that the collected signal power using our 2W probe laser was only about 0.02-0.04 W. On the positive side the surface was very uniform over a scan distance, with a signal variation of only about a factor of 2. Nevertheless for the demonstrations we were obliged to ground the surface near the cracks being scanned to enhance the reflectivity.

9.4.5 Scanning Platform

The scanning platform comprises of two flexible metal bands that wrap around the pipe. These bands act as the rails on which the two clamp-on linear actuators (bugs) are seated. A photo of one of the bugs is given in Figure 37. The setup is a modified version of equipment commonly used in automated welding and automated ultrasonic inspection of pipeline girth welds. These linear actuators move the sensor mounts along the circumference of the pipe. The two motors move in sync so as to maintain their circumferential orientation and precision.

A scanning rail with a lead screw is mounted onto the two bugs and acts as the rail for the sensor carriage. The lead screw moves the sensor carriage along the axis of the pipe. The sensor setups for the eddy-current mapping system as well as the laser ultrasonics measurement head are mounted onto the sensor carriage (Figure 38) using attachments that allow for proper positioning and alignment of the sensors for measurement. The axial rail also supports a flexible housing for the fiber-optic cables so as to maintain a desired bending ratio and prevent damage to the glass fibers.

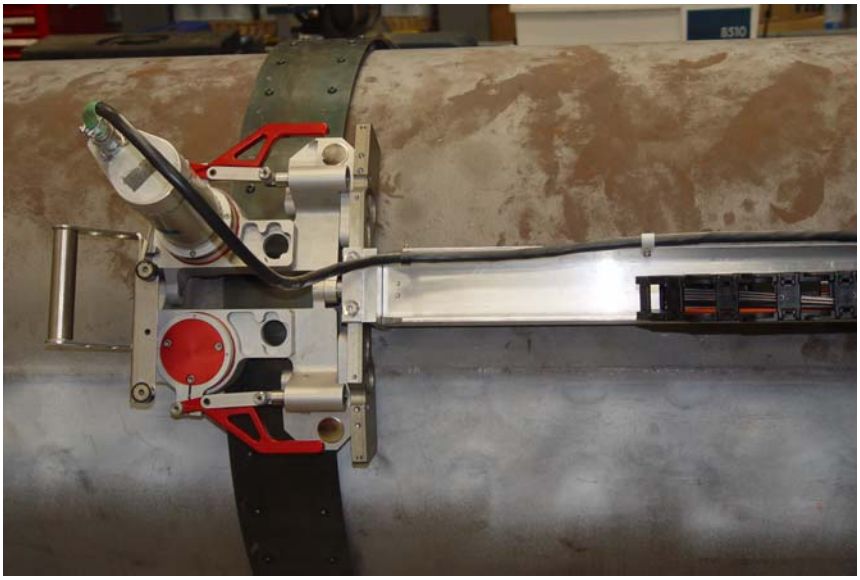

Figure 37 Photo of one of the bugs on the pipe.

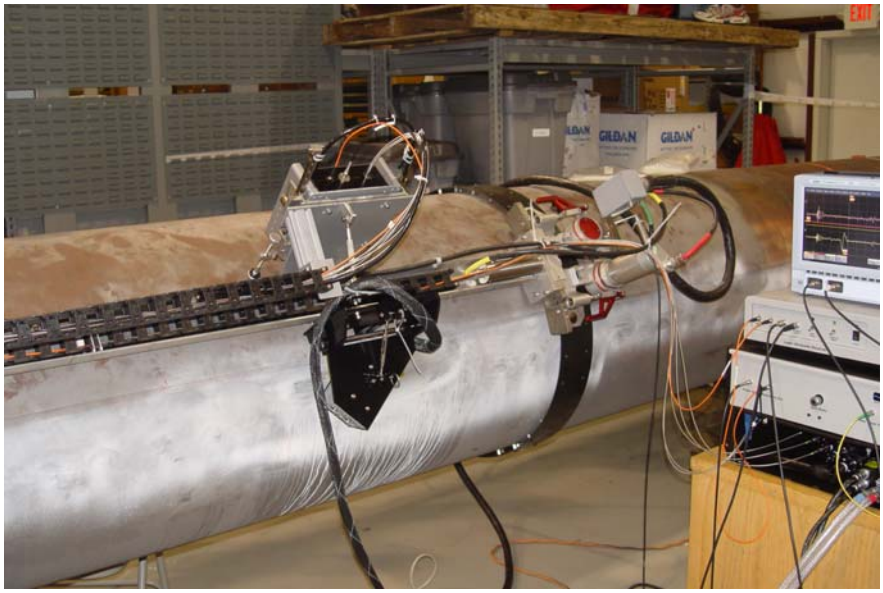

Figure 38 Photo of pipe with two sensors at the center and laser ultrasonic base station at right.

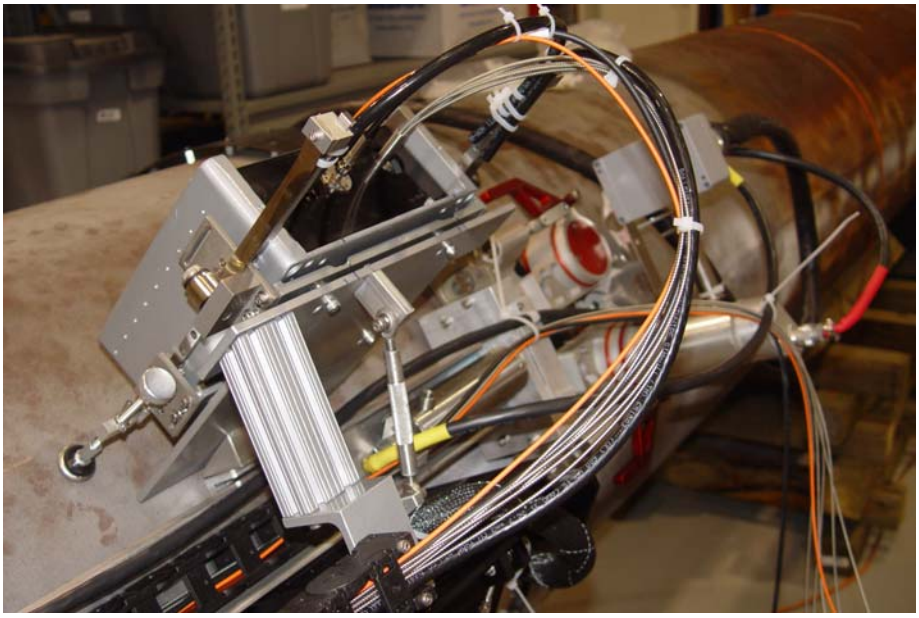

Figure 39 Close-up of laser ultrasonic head with associated fiber cables.

9.4.6 Testing and Demonstration

As part of the scope of work, three public demonstrations to industry were planned and executed (Figure 40). A 30 feet pipe sample affected with SCC was offered by one of the major North American pipeline operators for the purpose. The demonstrations were performed at the Applus RTD offices in Houston on July 23rd, August 6th and August 28th, to allow maximum participation from industry.

Figure 40 General view of demonstration setup.

The demonstration comprised of:

- A presentation explaining the need for such technology
- A presentation explaining the basic technology of laser ultrasonics
- A live demonstration of the scanner system using the eddy-current sensors for mapping SCC
- Real time extraction of the coordinates for the cracks that were picked for sizing using the laser ultrasonics system
- A live demonstration of the scanning system using laser ultrasonics for sizing SCC cracks identified within the colony
- Demonstration of the automated signal interpretation software

9.4.7 Crack Data

Over the course of the three demos we performed approximately 20 crack B-scans. One such B-scan is shown in Figure 41. The crack indications are (1) disturbance of the Rayleigh arrival and (2) delay of the surface-skimming longitudinal (SSL) wave. As indicated earlier, measurement of the SSL wave arrival time allows the determination of the crack depth. A separate software module performs this calculation. The result in this case is given in Figure 42. The two plot colors reflect different algorithms that were tried. Clearly the plot in red gives a smoother result.

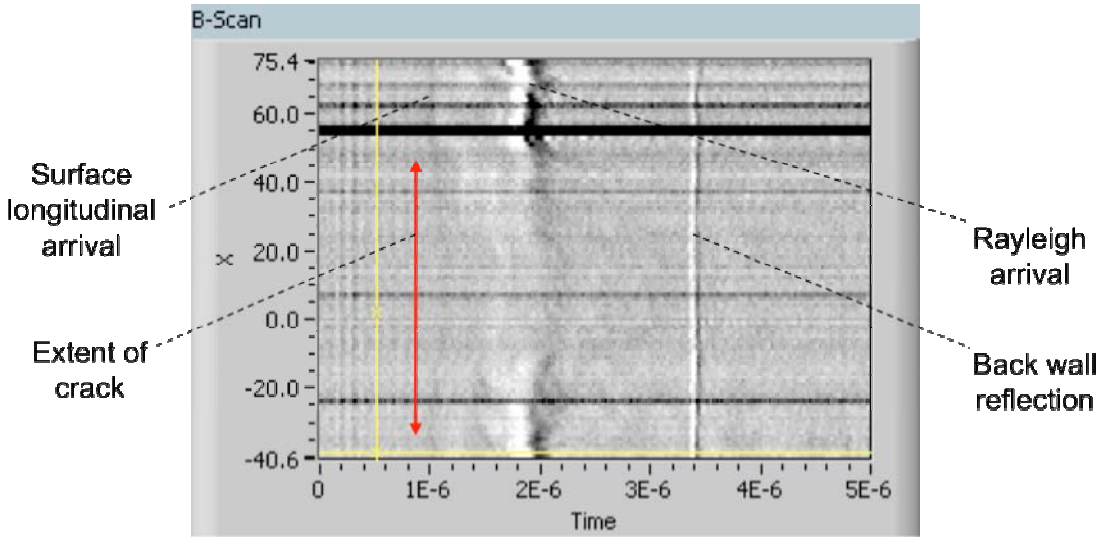

Figure 41 B-scan over crack on pipe. The extent of the crack is also shown.

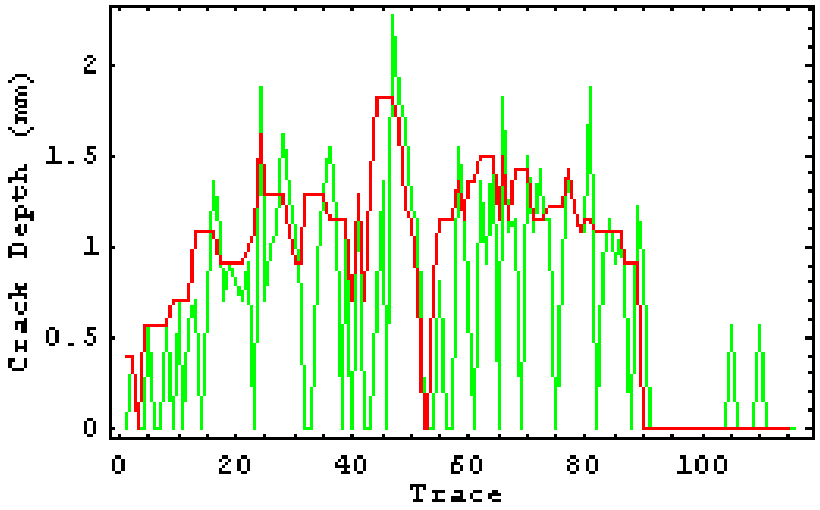

Figure 42 Software calculation of crack depth profile.

The data in Figures 41 and 42 can be combined to show the correlation between the B-scan and the crack profile, as shown in Figure 43. It can be seen that the crack profile correlates well with the disturbance of the Rayleigh wave and the delay of the SSL wave.

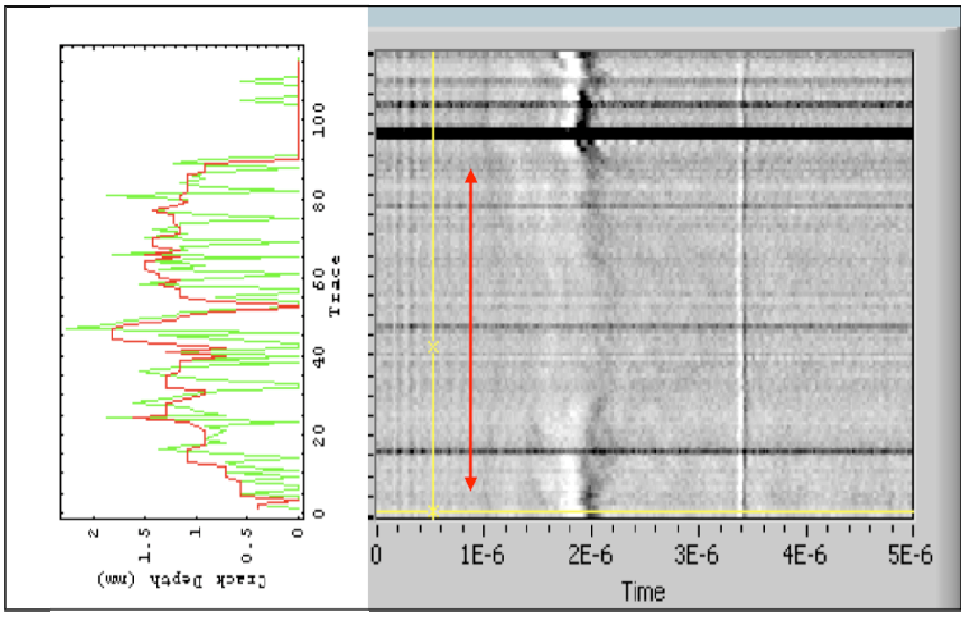

Figure 43 B-scan and crack depth profile.

9.4.8 Recommendations for Future Work

We can draw several conclusions regarding the technical and engineering performance of the laser ultrasonic system, as discussed below.

Fiber Delivery Of Generation Laser Pulses

Our five-fiber bundle scheme for delivery of the generation laser pulses to the pipe surface did not deliver as much laser energy to the surface as desirable for good signal-to-noise. In future

work we will use a turnkey integrated laser/fiber system with a specified 50 mJ in a 1 mm core fiber.

Probe Laser Power
The relatively low reflectivity of the sandblasted surface of the pipe does not provide sufficient power to our demodulator when using the 2W probe laser that we used at the demonstrations. We estimate that a 20W laser will be required.

Measurement Head
In light of the innovations that were integrated into the measurement head, the head performed very well. There was no sign of damage and the beams could be manipulated as expected from the design. We anticipate only incremental mechanical design improvements.

Crack Measurement Issues
On first examining the pipe chosen for the demos it became immediately clear that the SCC cracks in this pipe were more subtle than the cracks in the samples provided earlier to IOS for technology development. The prior samples had open cracks, while the cracks in the demo pipe were nearly invisible to the eye, although they were definitely observable by magnetic particle inspection and through MWM imaging.

Upon scanning the demo pipe cracks, we found that the normal ultrasonic signature formerly obtained with the lab samples was not always present. We suspected that some of the cracks were ultrasonically "partially transparent". If this interpretation is correct, then the signal-to-noise in our technique would be reduced. During the third demo we performed measurements on sections of the SCC colony that had been ground to improve the surface finish. It is possible that the grinding process closed the cracks and caused them to become partially transparent. We need to perform careful experiments on samples in our lab to better understand the ultrasonic signatures of realistic cracks with varying surfaces.

During the third demo we observed that the surface waves that we use to probe the cracks were being attenuated abnormally. We suspect that the grinding process had worked or smeared the surface in a way that added attenuation to the surface waves. This effect must also be examined.

ATTACHMENT 2
Summary Project Financials

The following table provides a summary of the financial status for the project:

Attachment 2
Project Financials (Final)
OTA DTPH56-06-T-000003

Actual costs for all particpants
Quarter 8

Milestone No.	Task	Budgeted milestone payments	Cumulative budgeted payments	Costs incurred	Cumulative costs incurred
			0.00		0.00
29	4	189,720.25	951,201.38	21,745.54	701,116.30
30	4	34,011.49	985,212.87	23,655.02	724,771.32
31	5	80,098.82	1,065,311.69	127,734.07	852,505.39

Cash cost share
Quarter 8

Milestone No.	Task	PRCI Forecast	PRCI Received	RTD Forecast	RTD Received	Total cost share forecast	Total Cost Share Received
29	4	1,298.54	0.00	155,708.76	0.00	157,007.30	0.00
30	4	1,298.54	0.00	0.00	0.00	1,298.54	0.00
31	5	1,298.54	0.00	20,000.00	0.00	21,298.54	0.00
		3,895.62	0.00	175,708.76	0.00	179,604.38	0.00

In kind cost share
Quarter 8

Milestone No.	Task	Forecast	Incurred
29	4	1,298.54	1,298.54
30	4	1,298.54	1,298.54
31	5	1,298.54	1,298.54
Quarter 8 Total:		3,895.63	3,895.63